Mon. Not. R. Astron. Soc. **000**, 1–**??** (2012) Printed 5 September 2012 (MN LaTeX style file v2.2)

arXiv:1209.0695v1 [astro-ph.CO] 4 Sep 2012

Automated measurement of redshift from mid-infrared low resolution spectroscopy

Antonio Hernán-Caballero

Instituto de Física de Cantabria, CSIC-UC, Avenida de los Castros s/n, 39005, Santander, Spain. E-mail: ahernan@ifca.unican.es

Accepted .... Received ....;

ABSTRACT

Obtaining accurate redshifts from mid-infrared (MIR) low-resolution (R ~ 100) spectroscopy is challenging because the wavelength resolution is too low to detect narrow lines in most cases. Yet, the number of degrees of freedom and diversity of spectral features are too high for regular spectral energy distribution (SED) fitting techniques to be convenient. Here we present a new SED-fitting based routine for redshift determination that is optimised for MIR low-resolution spectroscopy. Its flexible template scaling increases the sensitivity to slope changes and small scale features in the spectrum, while a new selection algorithm called Maximum Combined Pseudo-Likelihood (MCPL) provides increased accuracy and a lower number of outliers compared to the standard maximum-likelihood (ML) approach. Unlike ML, MCPL searches for local (instead of absolute) maxima of a "pseudo-likelihood" (PL) function, and combines results obtained for all the templates in the library to weed out spurious redshift solutions. The capabilities of MCPL are demonstrated by comparing its redshift estimates to those of regular ML and to the optical spectroscopic redshifts of a sample of 491 *Spitzer*/IRS spectra from extragalactic sources at $0 < z < 3.7$. MCPL achieves a redshift accuracy $\Delta(z)/(1+z) < 0.005$ for 78% of the galaxies in the sample compared to 68% for ML. The rate of outliers ($\Delta(z)/(1+z) > 0.02$) is 14% for MCPL and 22% for ML. χ^2 values for ML solutions are found to correlate with the SNR of the spectra, but not with redshift accuracy. By contrast, the peak value of the normalised combined PL (γ) is found to provide a good indication on the reliability of the MCPL solution for individual sources. The accuracy and reliability of the redshifts depends strongly on the MIR SED. Sources with significant polycyclic aromatic hydrocarbon emission obtain much better results compared to sources dominated by AGN continuum. Nevertheless, for a given γ the frequency of accurate solutions and outliers is largely independent on their SED type. This reliability indicator for MCPL solutions allows to select subsamples with highly reliable redshifts. In particular, a $\gamma > 0.15$ threshold retains 79% of the sources with $\Delta(z)/(1+z) < 0.005$ while reducing the outlier rate to 3.8%.

Key words: catalogues – galaxies: distances and redshifts – infrared:galaxies – methods: data analysis

1 INTRODUCTION

Finding a galaxy's redshift typically requires the identification of narrow emission or absorption lines in a medium- or high-resolution spectrum (spectroscopic redshift). Alternatively, broad features of the spectral energy distribution (SED) are revealed by multi-wavelength photometry, and can be used to obtain photometric redshifts. Spectroscopic redshifts are accurate but very time-consuming, while photometric redshifts offer limited accuracy (typically in the $\Delta z/(1+z) \sim 0.01$–0.1 range) and suffer from color degeneracies that may lead to catastrophic errors (Fernández-Soto et al. 1999; Benítez 2000).

Halfway between the two is low resolution spectroscopy (LRS), which at R ~ 50–100 provides a compromise between sensitivity and spectral resolution. LRS has become common in space based infrared missions, particularly *Spitzer* with the Infrared Spectrograph (IRS; Houck et al. 2004), and later AKARI and its Near-infrared Camera/spectrometer (IRC) (Onaka et al. 2007; Murakami et al. 2007).

Future infrared missions will also provide LRS capabilities, including the Mid-InfraRed Instrument onboard JWST (MIRI; Wright et al. 2008) and two instruments for SPICA: the Mid-InfRAred Camera w/wo LEns (MIRACLE; Wada & Kataza 2010) and the far-infrared instrument (SAFARI; Goicoechea et al. 2011).

Since the spectrum is spread over a smaller number of pixels, mid-infrared (MIR) 5–35 μm LRS offers higher continuum sensitivity with a spectral resolution still capable of resolving many features used for diagnostics, like the polycyclic aromatic hydrocarbon (PAH) bands and absorption bands from silicates, water ice, and carbon monoxide, among others.

LRS has also the potential to yield redshifts with accuracies intermediate between those of medium resolution spectroscopy and photometric redshifts, since the theoretical redshift resolution is proportional to the wavelength resolution: $\Delta z/(1+z) \sim \Delta\lambda/\lambda$. Nevertheless, narrow spectral lines are marginally unresolved at LRS resolutions, and this outweighs for them the sensitivity advantage over higher resolution spectroscopy, since the lines get washed out by the continuum emission. Because of this dilution, narrow lines are clearly detected only in high signal to noise ratio (SNR) spectra or in sources with large equivalent width (EW). Therefore, fine structure lines observed at LRS are not suitable for spectroscopic redshift determination in the general case.

In MIR spectra, the PAH and silicate bands are routinely used to estimate the redshifts of optically faint sources (e.g. Houck et al. 2007; Yan et al. 2007; Farrah et al. 2009; Weedman et al. 2009). However, since they often show complex morphologies, it requires a visual inspection to properly identify them, particularly in sources with high obscuration or where a strong active galactic nucleus (AGN) continuum reduces the contrast of the features. In addition, spectra with low SNR make it difficult to identify individual features even to the trained eye.

When spectroscopic redshifts are not workable, the backup strategy is photometric redshifts. The multiple photometric redshift techniques developed can be classified in two main groups: those based on "learning" with a large training set (e.g. Connolly et al. 1995; Brunet et al. 1997; Wang et al. 1998; Collister & Lahav 2004; Wadadekar 2005; Carliles et al. 2010) and those based on "SED-fitting" with a set of spectral templates (e.g. Baum 1962; Koo 1985; Lanzetta et al. 1996; Gwyn & Hartwick 1996; Sawicki et al. 1997; Fernández-Soto et al. 1999; Benítez 2000; Bolzonella et al. 2000; Le Borgne & Rocca-Volmerange 2002; Babbedge et al. 2004; Feldmann et al. 2006).

SED-fitting works well with broadband photometry in the optical and near-infrared (NIR) because the SED of galaxies in this range shows little diversity. In normal galaxies the SED is dominated by starlight, and it can be successfully modelled by the combination of a few stellar populations obscured by a screen of dust (e.g. Bruzual & Charlot 1993, 2003; Silva et al. 1998) or compared to a small set of empirical (e.g. Assef et al. 2008) or semi-empirical (e.g. Coleman et al. 1980; Ilbert et al. 2006) templates.

Even if the galaxy hosts a low luminosity AGN or an obscured AGN of any luminosity, it has little impact on the broadband SED of the galaxy. Only quasars produce continuum emission strong enough to dominate the optical-NIR SED of the galaxy, and they become a hassle for photometric redshift routines (Hatziminaoglou et al. 2000; Richards et al. 2001). This is because their power-law SED does not provide high contrast features, and the broad emission lines require good coverage with narrow or intermediate band filters to be identified (Benítez et al. 2009; Matute et al. 2012; Abramo et al. 2012)

In the MIR, SED-fitting is far more problematic because the output of galaxies arises from several independent processes, including the Rayleigh-Jeans tail of stellar emission, thermal emission from hot and warm dust heated by the (active) nucleus, fluorescence of PAH molecules, radiative transitions of ionised and neutral atoms, rotational and vibrational transitions of H_2 and other molecules, and non-thermal radiation from radio sources (AGN, supernovae, masers).

Furthermore, there is high dispersion in the correlation between emission from the stellar component and the interstellar medium, and population synthesis codes do not yet reproduce accurately spectral features at wavelengths $\lambda \gtrsim 5$ μm , in particular PAH emission (Brodwin et al. 2006). In practice, adding photometric points at wavelengths $\lambda \gtrsim 5$ μm to an optical-NIR SED does not improve the accuracy of the redshift solution. Nevertheless, Rowan-Robinson et al. (2008) successfully apply a two-step method to fit photometry longward and shortward of 5 μm with to separate set of templates, and Negrello et al. (2009) obtain $\Delta(z)/(1 + z) < 0.1$ for 90% of sources in the range $0.5 < z < 1.5$ using a combination of *ISO*, *Spitzer*, and *AKARI* photometry in the 3.6–24 μm range.

Template fitting can produce very accurate redshift estimates with MIR LRS if one important issue is addressed. Because of the diversity of MIR SEDs and the large number of data points in the spectrum (compared to photometric SEDs), it cannot be expected that every source in a survey will find an accurate model of its MIR SED in the template library. As a consequence, the standard approach of SED-fitting photometric redshifts (that is, shifting and scaling of the template, and a χ^2 minimisation to find the best fit) needs to be modified. This is because it favours the templates that best reproduce the overall shape of the continuum even if the smaller scale features (the ones capable of producing an accurate redshift) are poorly fit or misplaced.

A good match at certain redshift between small scale spectral features of the spectrum and a template will be signaled by a sudden drop in the value of the χ^2 statistics relative to values for similar redshifts. This may not be the absolute minimum in χ^2 if the shape of the continuum is somewhat different for the spectrum and template, and there may be more than one such dips if one or more features produce partial matches by chance.

In addition, it is likely that several templates have at least some features in common with the spectrum. Each of them will produce a drop in χ^2 at the actual redshift of the source, while spurious alignments can occur at different redshifts for each template. Thus, filtering the redshift values at which different templates obtain local minima of χ^2, and then combining them in a way that favours strong dips as well as frequently repeated redshifts, allows to obtain a redshift solution that is much more robust than finding the absolute minimum of χ^2 for any template.

In this work a routine for redshift estimation from MIR LRS based on these principles is presented, and its capabilities demonstrated using a large sample of extragalactic sources with both optical and *Spitzer*/IRS spectroscopy.

The outline of the paper is as follows. Section 2 presents the algorithm for redshift estimation and explains the features that depart from regular χ^2 minimisation routines. §3 describes the sample selection and §4 the template library. §5 evaluates the accuracy and reliability of the redshift estimates obtained and their dependency with the MIR type of the source. §6 briefly summarizes the main conclusions of the paper.

2 THE METHOD

The redshift determination algorithm described here is implemented by the *Redshift COde for LOw-Resolution Spectroscopy* (*z*COLORS), developed by the author. It obtains the redshift of a source as well as an estimate of its reliability by comparing its MIR spectrum (hereafter, the spectrum) with a set of spectral templates (hereafter, the templates).

Let F(λ) be the flux density of the spectrum as a function of the observed wavelength λ, and $S_k(\lambda')$ the flux density of the *k*-th template as a function of the restframe wavelength λ'.

Both the spectrum F(λ) and templates $S_k(\lambda')$ are resampled to a common grid of wavelength values $\lambda_i = \lambda_0 e^{\beta i}$. The parameter β determines the spectral resolution R = $1/\beta$ of the resampled spectrum and templates. The uniform spacing in $\log\lambda$ is convenient for computational efficiency reasons, since such sampling ensures that the set of redshift values $z_j = e^{\beta j} - 1$, also evenly spaced in $\log(1+z)$, verifies $\lambda_{i+j} = \lambda_i(1+z_j)$ for every {i, j}. This allows to obtain the observed frame templates for redshift z_j, sampled at the same wavelengths as F(λ), by just shifting one position the indices of the templates for z_{j-1}, with no need for a new resampling or interpolation.

For every redshift z_j and template k, the routine performs a least squares fit in which the template flux is scaled to fit the spectrum. Since the overall continuum slope provides little information on the redshift of the source, the flexibility of the fit is increased by allowing for a wavelength-dependent scaling factor. That is, the spectrum F(λ) is fitted to a function of the form:

$$f_k(\lambda, z_j) = (a_k(z_j) + b_k(z_j)\cdot\log\lambda)\cdot S_k\Big(\frac{\lambda}{1+z_j}\Big) \quad (1)$$

where a, b are free parameters.

This flexible scaling helps the templates obtain better fits even if their continuum slope is somewhat different from that of the spectrum. As a consequence the fit becomes more sensitive to small scale features in the spectrum.

In a standard template fitting, the goodness of fit is quantified by the reduced χ^2 statistics:

$$\chi^2_k(z_j) = \frac{1}{N_{jk}-2}\sum_i^{N_{jk}}\left(\frac{F(\lambda_i) - f_k(\lambda_i, z_j)}{\sigma_i}\right)^2 \quad (2)$$

where N_{jk} is the number of λ values in which the (resampled) spectrum and the redshifted template k overlap at redshift z_j, and σ_i is the one sigma uncertainty in $F(\lambda_i)$.

The likelihood of a given redshift and template pair (z, T) is then $\mathscr{L}_T(z) \propto e^{-\chi^2_T(z)}$, and assuming all templates and redshifts have the same probability *a priori*, the maximum likelihood (ML) solution is simply the (z, T) pair that maximizes $\mathscr{L}_T(z)$.

The ML solution also assumes that the template set is exhaustive (includes all possible types), but this condition is difficult to meet with samples of MIR spectra because of the high number of physical processes involved.

When none of the templates is an accurate model of the spectrum, the χ^2 minimisation favours those templates that best reproduce the overall shape of the continuum even if small scale features are poorly fit, simply because the latter only affect a small fraction of the λ_i. Such behaviour is unwelcome, since the narrow spectral features are crucial to obtain an accurate redshift estimate, while the continuum curvature and slope changes only provide rough redshift indications.

To overcome this limitation, we propose a new algorithm for finding the most probable redshift value, called "maximum combined pseudo-likelihood" (MCPL).

The main features of MCPL are: a) it searches for local – instead of absolute– maxima in $\mathscr{L}_T(z)$; b) it combines information on the local maxima found by all templates to produce a pseudo-likelihood distribution as a function of redshift.

The rationale behind this approach is that the broadband SED of the source determines the general shape of $\mathscr{L}_T(z)$, while narrow spectral features cause high frequency variations in $\mathscr{L}_T(z)$ as they correlate (or not) with features in the template. A good correlation of several features at a certain redshift produces a sharp peak in $\mathscr{L}_T(z)$ that signals a candidate redshift solution. The spurious alignment of a few features or noise spikes in the spectrum and the template can also produce a peak in $\mathscr{L}_T(z)$ at a wrong redshift. This peak can even be higher than the $\mathscr{L}_T(z)$ value at the actual redshift if the template is a poor model for the spectrum. However, such chance alignments tend to appear at different redshift for each template, while the legitimate peak always occurs at the same (actual) redshift. Because of this, combining information on the position and strength of local maxima produced by all the templates has the potential to yield a more robust redshift estimate compared to considering only the best fitting template.

This idea is implemented by a "filter" function that zeroes all values of $\mathscr{L}_T(z)$ except those corresponding to local maxima:

$$\mathscr{L}^*_T(z) = \begin{cases}\mathscr{L}_T(z) & \text{if local maximum}\\ 0 & \text{otherwise}\end{cases} \quad (3)$$

The combined, filtered likelihood distribution is then the sum over all the templates:

$$\mathscr{L}^*(z) = \sum_i^{N_T} \mathscr{L}^*_i(z) \quad (4)$$

The filtering implies that each template promotes only those redshift values at which it finds a (partial) correspondence of features with the spectrum.

The information provided by the continuum is not lost, though, since the height of the local peaks in $\mathscr{L}_T(z)$ still indicates the goodness of fit between spectrum and template at those particular redshifts.

Since the template set cannot reproduce all the possible combinations of spectral features (that is, it is not complete), even the best fitting template at the correct redshift is not in general an accurate model for the intrinsic spectrum of the source. In other words, the differences between spectrum and template cannot be accounted for by flux uncertainties alone. Therefore, the reduced χ^2 increases with increasing SNR, and produces $\chi^2 \gg 1$ even for fits that a visual inspector would consider very good.

The exponential dependency of $\mathscr{L}$ with χ^2 implies that the peak with lowest χ^2 usually dominates the resulting combined $\mathscr{L}^*(z)$, making the contribution from other peaks negligible and turning the MCPL algorithm into simple ML.

To overcome this undesired effect, the likelihood function $\mathscr{L}$ can be substituted with a "pseudo-likelihood" q that is proportional to the inverse of the reduced chi-squared statistics:

$$q_T(z) = \frac{a(z, T, \theta)}{\chi^2_T(z)} \quad (5)$$

where the *prior* $a(z, T, \theta)$ captures all the information about the source to be weighted in the selection of the best redshift estimate, such as the observed flux density in a given band, or the *a priori* probability of any (z, T) combination.

Using $q_T(z) \propto 1/\chi^2_T(z)$ instead of $\mathscr{L}_T(z) \propto e^{-\chi^2_T(z)}$ still favours the lowest value of χ^2, but lets other local peaks have some influence on the final solution.

The "combined pseudo-likelihood" function $Q(z)$ is then defined as:

$$Q(z) = \sum_i^{N_T} q^*_i(z) \quad (6)$$

where $q^*_i(z)$ is the filtered $q_T(z)$ for template i in which all values other than local maxima have been zeroed.

Variations among templates in the profile of a resolved spectral feature like the 7.7 μm PAH complex or the ∼10 μm silicate feature cause that different templates produce peaks at slightly different redshifts. This results in tight clusters of nearby peaks in the combined $Q(z)$. If the redshift difference between the peaks in a cluster is comparable to the theoretical redshift resolution the spectrum is capable of, it can be assumed that all these peaks represent the same redshift solution, although with some dispersion.

To compensate for this, $Q(z)$ is convolved with a gaussian kernel (whose full width at half maximum is twice the redshift resolution) to produce a smoothed $Q_s(z)$. The final solution is then the redshift $z_{\rm best}$ that maximizes $Q_s(z)$.

In regular SED-fitting ML photometric redshifts, error bars for the redshift estimate can be computed using the $\Delta\chi^2$ method (e.g. Anvi 1976; Bolzonella et al. 2000). This method assumes the probability distribution for the minimum of $\chi^2(z)$ ($\chi^2_{\rm min}$) is the χ^2 distribution for n degrees of freedom (Press et al. 1992). Nevertheless, even for broadband photometric redshifts the χ^2 distribution is not a realistic description of the actual redshift uncertainties, because the model is not linear in the fitting parameters (namely, the redshift) and there are degeneracies between redshift and galaxy SED types (Oyaizu et al. 2008).

Like $\chi^2_{\rm min}$, the peak value of $Q_s(z)$ depends mainly on the SNR of the spectrum, and does not provide a direct estimation of the reliability of the redshift solution. Still, our results with MIR spectra indicate that the value of $Q_s(z_{\rm best})$, if normalised to the integral over the entire range of redshifts:

$$\gamma = Q_s(z_{\rm best})/I, \qquad I = \int_{zmin}^{zmax} Q_s(z')dz' \qquad (7)$$

provides valuable information regarding the strength of the redshift solution. A value of γ close to 1 indicates that the peak at $z_{\rm best}$ clearly dominates the $Q_s(z)$ distribution, and thus the redshift estimate should be reliable. Conversely, a very low γ indicates that there are many secondary peaks with similar strength, and the redshift estimate is unreliable.

Another related parameter, useful to estimate the degree of degeneracy, is the ratio R between the $Q_s(z)$ values for the highest and second-highest peaks. A ratio close to 1:1 indicates peaks of comparable strength and reveals a significant probability of catastrophic redshift error.

3 SAMPLE SELECTION

The spectra used here were selected from the *Spitzer*/IRS ATLAS project (ATLAS-IRS, Hernán-Caballero & Hatziminaoglou 2011), which compiles MIR spectra and ancillary data from 739 extragalactic sources at $0 < z < 3.7$.

The parent sample is composed of all the ATLAS-IRS sources with a known spectroscopic redshift from optical or near-infrared spectroscopy ($z_{\rm spec}$). To ensure enough spectral coverage, 20 sources observed in only one of the four IRS modules were discarded. 11 additional sources where selected as templates (see §4) and removed from the sample to avoid circularity issues.

The information content in each spectrum was computed using the net significance ($\mathscr{N}$), defined as the maximum cumulative SNR of the spectrum (Pirzkal et al. 2004). The 3 sources with lowest net significance values ($\mathscr{N} < 100$, corresponding to median SNR per pixel $\lesssim 0.8$) were also removed from the sample.

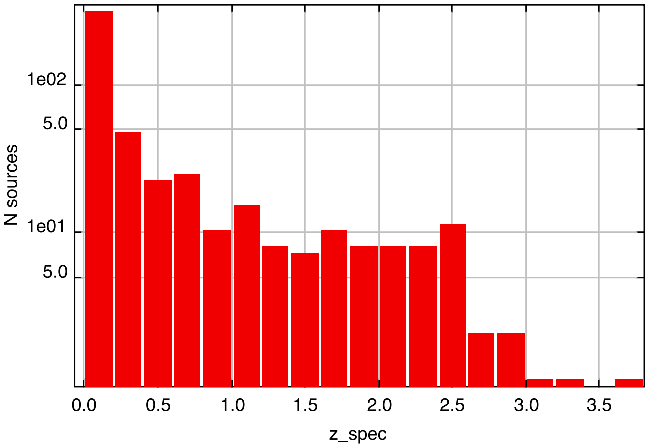

Figure 1. Redshift distribution for the 491 sources in the main sample.

The remaining 491 sources constitute the main sample of this work. Their redshift distribution is shown in Figure 1.

About half of the sample is at redshift $z_{\rm spec} < 0.15$, while only ∼20% is at $z_{\rm spec} > 1$. This distribution is similar to that of the entire set of extragalactic sources with *Spitzer*/IRS spectroscopy and known spectroscopic redshifts (Lebouteiller et al. 2011).

321 sources (65% of the sample) are classified as AGN in the optical, including 124 optical quasars (QSO), 46 obscured quasars (QSO2), 12 type 1 Seyferts (Sy1), 73 intermediate type Seyferts (Sy1.X), 60 type 2 Seyferts (Sy2), and 56 LINERs.

In the MIR, 285 sources (58% of the sample) are classified as AGN-dominated, while 181 are starburst-dominated and 10 are classified as composites with roughly equal contributions from the AGN and starburst to the infrared output of the galaxy. See Hernán-Caballero & Hatziminaoglou (2011) for further details on the optical and MIR classifications.

4 TEMPLATES

To obtain reliable redshift estimates, it is essential that the templates cover as much as possible the restframe spectrum of the source at any redshift, since insufficient overlap between spectrum and template increases the probability of obtaining a good fit at a wrong redshift due to chance alignments of spectral features.

For spectra observed in the four IRS channels (5–35 μm), a redshift search range $0 < z < 4$ implies that the templates should ideally span the entire 1–35 μm restframe range. In practice, shorter wavelength coverage suffices, as long as the template and spectrum share enough overlap in the entire redshift search range.

A large number of spectral templates were generated based on IRS spectra from ATLAS-IRS and from the Cornell Atlas of Spitzer/IRS Spectra (CASSIS; Lebouteiller et al. 2011) using several methods:

a) for a sample of local luminous and ultra-luminous infrared galaxies, their AKARI 2.5–5 μm spectrum (Imanishi et al. 2010) is used to extend their IRS spectrum down to restframe ∼ 2 μm. b) composite spectra of several samples of $z > 1$ quasars (selected by their restframe 3.6 to 5.6 μm continuum slope and/or strength of the silicate feature) are used to extend the IRS spectrum of individual, lower redshift quasars with good SNR. c) individual and composite spectra of $z > 0.5$ radiogalaxies are used to extend individual spectra of low redshift radigalaxies. d) another template is produced

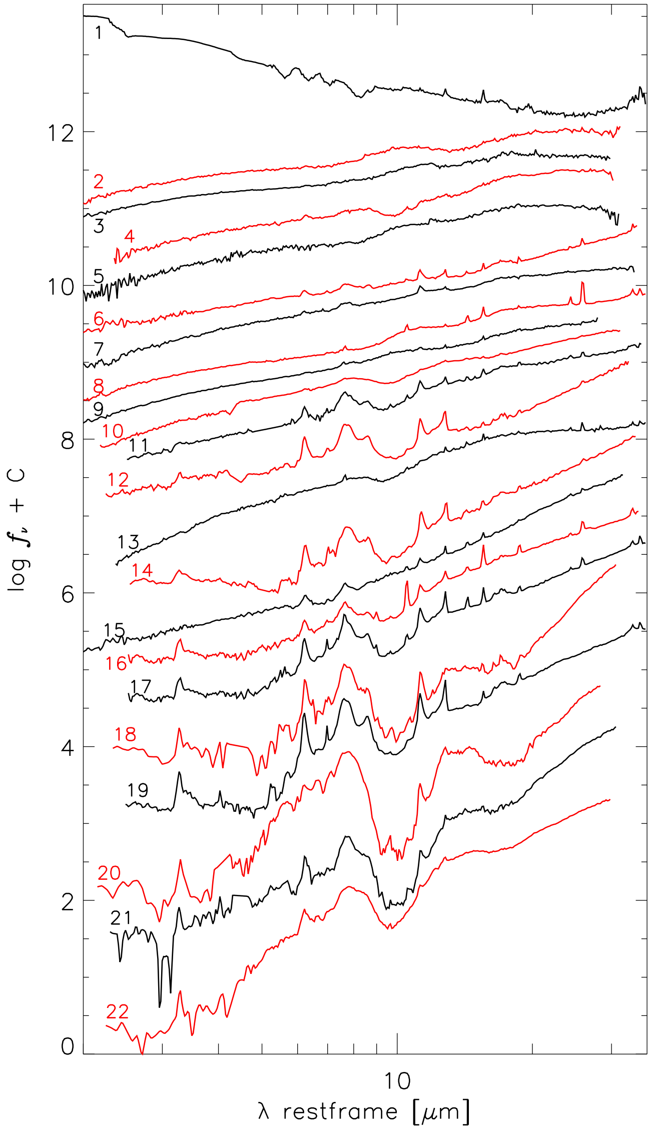

Figure 2. The 22 spectral templates used by the SED-fitting routine, ordered by increasingly red continuum. Numbers correspond to row indices in table 2. Alternative red and black colours are used for clarity only.

from the composite spectra of radiogalaxies with strong emission in the [SIV] 10.51 μm line. e) An early-type non-active galaxy template is obtained by extending the IRS spectrum of NGC 5011 with the elliptical galaxy template from Coleman et al. (1980).

In addition, archival *ISO*/SWS 2–45 μm spectra of NGC1068, M82, and the Circinus galaxy are also included as templates.

A selection procedure was devised to identify the best performing templates. First, the filtered pseudo-likelihood function, $q_{i,j}(z)$, is calculated for every pair $\{i,j\}$ of template and spectrum. Then, subsets of templates are given a score based on the number of accurate $(\Delta z/(1+z) < 0.01)$ redshift solutions obtained with that particular subset. A penalisation factor depending on the number of templates is also included to discourage large template sets.

An iterative process finds the subset that maximizes the score by randomly adding or removing one or several templates to the subset, keeping only those changes that increase the score until no further increases are possible. This process is run several times to ensure it always converges to the same template set.

Note that since the MCPL redshift solution for any source depends on the whole template set (and not just the template obtaining the best fit) the optimisation would discard a template that produces good fits for a few unusual sources if it degrades the solution for many others. Nevertheless, it is unlikely that a chance alignment of some features in a template that does not match the overall SED of a source can produce a peak in $q_{i,j}(z)$ strong enough to overshadow the combined peaks produced by the remaining templates at the actual redshift.

The final set, containing 22 templates, is shown in Figure 2 and listed in Table 2. The templates derived from spectra of sources in the sample produce, as expected, very good fits for these particular sources. To avoid misrepresenting the actual accuracy of the method, these sources are removed from the sample.

5 RESULTS

*z*COLORS was run on the sample of 491 spectra selected from ATLAS-IRS with the template set described in the previous section.

The spectra and templates are resampled to a constant spectral resolution $R = 500$, which provides a redshift resolution $\frac{\Delta z}{1+z} = 0.002$. In test runs, higher resolution values increase the computational cost with no significant gain in accuracy of the redshift solutions. The search range for redshifts is $-0.05 \leqslant z \leqslant 4$, with the extension to small negative values being important to properly identify the peak of $q_T(z)$ in nearby galaxies ($z \sim 0$).

All templates are assumed to have the same *a priori* probability. The only *prior* introduced is a luminosity limit, aimed at preventing bright sources from obtaining high redshift estimates that would imply unrealistically high luminosities. The luminosity limit is conservatively put at $\nu L_\nu = 5{\times}10^{47}$ erg s^{-1}, which is just above the most luminous source in the sample. For every source, the redshift ($z_{\rm cut}$) corresponding to this luminosity is found, and the *prior* $a(z)$ is then defined by:

$$a(z) = \begin{cases} 1 & \text{if } z \leqslant z_{\rm cut} \\ 0 & \text{if } z > z_{\rm cut} \end{cases} \qquad (8)$$

The luminosity limit achieves a ~30% reduction in the number of catastrophic errors $(\Delta z/(1+z) > 0.1)$ relative to a flat *prior*. This suggests a more elaborate *prior* including luminosity limits that depend on the SED and observed flux of the source could probably help to further reduce degeneracies.

Table 1 contains the redshift solutions obtained by the ML and MCPL algorithms for all the sources in the sample.

5.1 Accuracy of redshift solutions

The accuracy of the $z_{\rm IRS}$ estimates is evaluated by comparing them to the redshifts from optical or NIR spectroscopy ($z_{\rm spec}$). The error in the $z_{\rm IRS}$ value is represented by $d = (z_{\rm IRS} - z_{\rm spec})/(1 + z_{\rm spec})$ and its modulus, $\delta = |d|$, defines the accuracy of the redshift solution.

Figure 3 shows the correlation between $z_{\rm IRS}$ and $z_{\rm spec}$ values for both, the ML and MCPL selection algorithms. 86% of MCPL solutions and 78% of ML are enclosed within the parallel lines that represent accuracy $\delta < 0.02$, but typical accuracies are much higher.

The number of outliers ($\delta > 0.02$) is 69 for MCPL and 106 for ML. Excluding them, errors for MCPL (ML) solutions average $2.0{\times}10^{-5}$ ($-4.5{\times}10^{-5}$) with a standard deviation of 0.0033 (0.0046). This indicates there is no significant bias in the redshift estimates

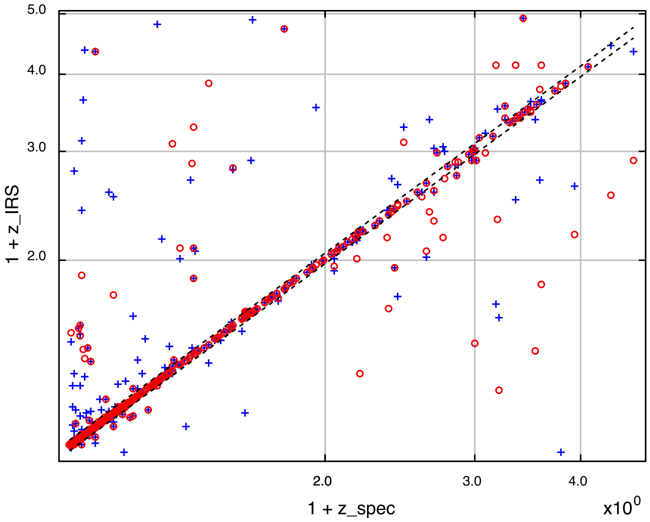

Figure 3. Comparison between the redshifts derived from template fitting ($z_{\rm IRS}$) and those from optical spectroscopy ($z_{\rm spec}$). Plus signs mark solutions from the ML algorithm, while open circles mark those of the MCPL selection algorithm. The dotted lines enclose those sources with redshift accuracy $\delta < 0.02$.

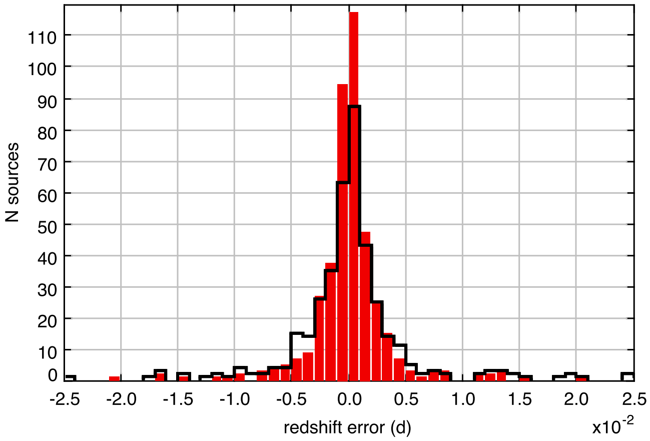

Figure 4. Distribution of redshift errors ($d = (z_{\rm IRS} - z_{\rm spec})/(1 + z_{\rm spec})$) obtained using the ML (solid line) and MCPL (solid bars) selection algorithms.

and the typical errors are just a fraction of the spectral resolution of IRS ($\delta\lambda/\lambda \sim 0.008$–$0.016$, depending on wavelength). The distribution of redshift errors is approximately gaussian, with full width at half maximum 0.0047 for MCPL and 0.0056 for ML (see Figure 4).

The cumulative distribution of δ for MCPL and ML solutions is presented in Figure 5. Both distributions show similar trends, with a rapid growth in the number of sources up to $\delta \sim 0.005$ and much slower growth at higher values. The curve for MCPL is consistently over ML in the entire δ range, but the separation is larger at $\delta \sim 0.005$. The number of sources in the range $0.02 < \delta < 0.1$ is 52 for ML versus 29 for MCPL, indicating a higher prevalence of low accuracy solutions in ML. Catastrophic redshift errors ($\delta > 0.1$) are obtained in 40 and 54 sources for MCPL and ML, respectively.

Comparison of ML and MCPL solutions for individual sources reveals that in 2/3 of the sample (318 sources) δ values from both algorithms are within 10% of each other. In another 132 sources the MCPL solution is clearly more accurate (sometimes by several orders of magnitude), while only in 37 cases is the ML significantly better.

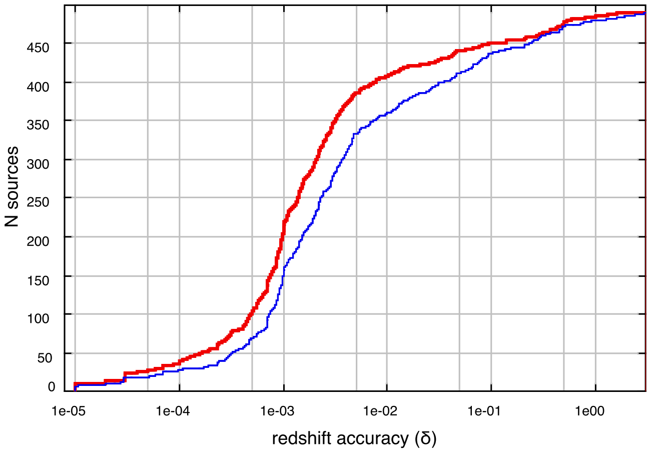

Figure 5. Cumulative distribution of the accuracy parameter $\delta = |z_{\rm IRS} - z_{\rm spec}|/(1{+}z_{\rm spec})$.The thin solid line represents results for the ML selection algorithm while the thick solid line corresponds to those of the MCPL algorithm.

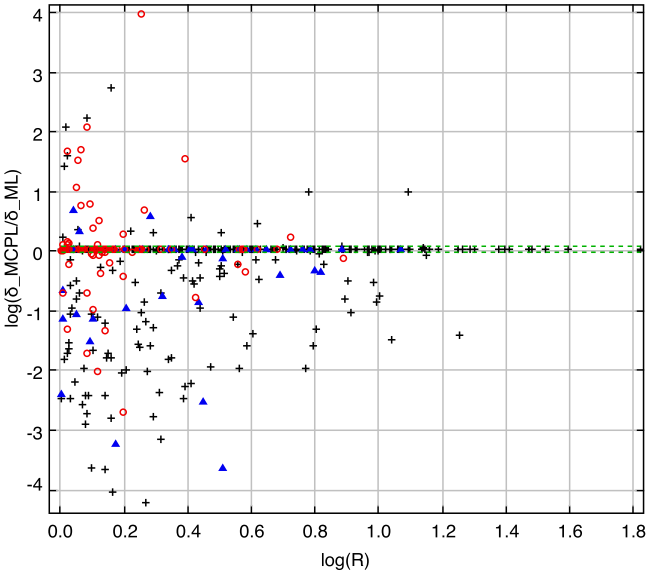

Figure 6. Logarithm of the ratio between accuracies of the MCPL and ML redshift solution versus degeneracy parameter (R) of the MCPL solution for sources at $z_{\rm spec} < 0.5$ (plus signs), $0.5 < z_{\rm spec} < 1$ (solid triangles), and $z_{\rm spec} > 1$ (open circles). Negative values indicate a higher accuracy for the MCPL solution compared to ML. The dotted lines enclose the region corresponding to MCPL and ML solutions within 10% of each other, which contains 65% of the sources in the sample.

The accuracy advantage of MCPL over ML is clearer at low redshift: at $z < 0.5$ MCPL outperforms ML in 96 cases versus 16 for ML, while at $z > 1$ they are levelled, with each of them wining in 19 cases. This is probably a consequence of the decrease in the average SNR with redshift. A lower SNR reduces the contrast of the legitimate peak in $Q_s(z)$ and makes it easier for spurious peaks to obtain comparable strength, increasing the risk of degeneracies.

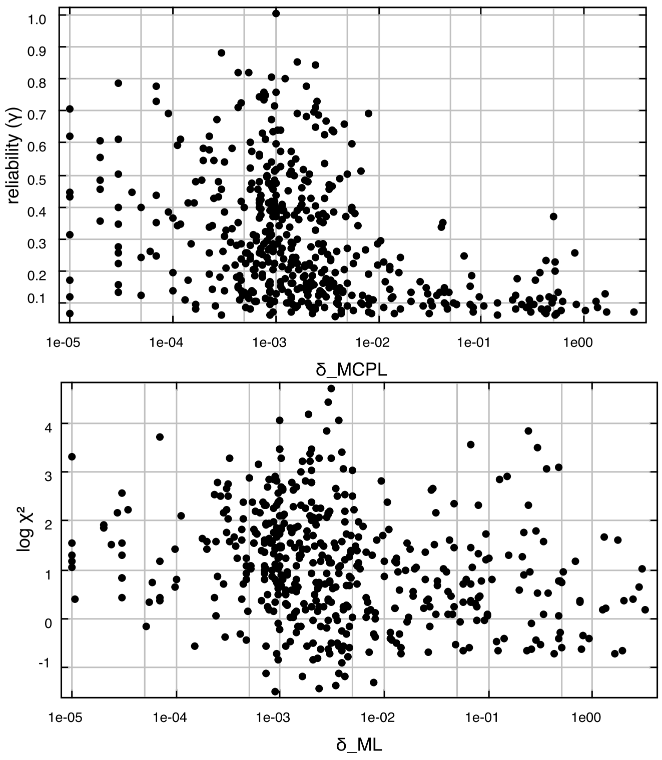

Figure 7. Top: relation between reliability (γ) and accuracy (δ) parameters for MCPL solutions. Bottom: logarithm of the reduced χ^2 statistic versus δ for ML solutions.

Figure 6 represents the ratio between δ values of the MCPL and ML solutions versus the "degeneracy parameter" (R), defined as the ratio between the highest and second highest peaks in $Q_s(z)$. Most sources with ML solutions significantly more accurate than MCPL have log(R) < 0.15, indicating an extreme degree of degeneracy in $Q_s(z)$. In these sources, the two highest peaks in $Q_s(z)$ have very similar strength, and it is thus no surprise that MCPL chooses sometimes the wrong one. Nevertheless, even with a very degenerate $Q_s(z)$ MCPL offers higher reliability than ML: from 138 sources with log(R) < 0.15, the MCPL solution is accurate ($\delta < 0.02$) while ML is an outlier ($\delta > 0.02$) in 26 cases, versus only 7 the other way around. In another 63 cases both are accurate and in the remaining 40 both are outliers.

5.2 Reliability of individual solutions

Apart from obtaining a high rate of accurate solutions, it is important to know the reliability of individual solutions. In §2 we anticipated that the γ parameter can provide such information for the MCPL algorithm.

The upper panel in Figure 7 represents γ versus δ for the MCPL solutions of the 491 sources in the sample. Accurate solutions obtain γ values spanning the whole ~0.05–1 range, while outliers concentrate at $\gamma \lesssim 0.15$, with few cases above that value.

Table 3 demonstrates that the reliability of MCPL solutions increases monotonically with γ, both in terms of the dispersion and median of δ values and in the frequency of outliers. This implies that by setting an appropriate threshold value for γ and selecting only the sources that surpass it, it is possible to obtain subsamples of sources with very reliable redshift estimates, albeit at a cost in completeness.

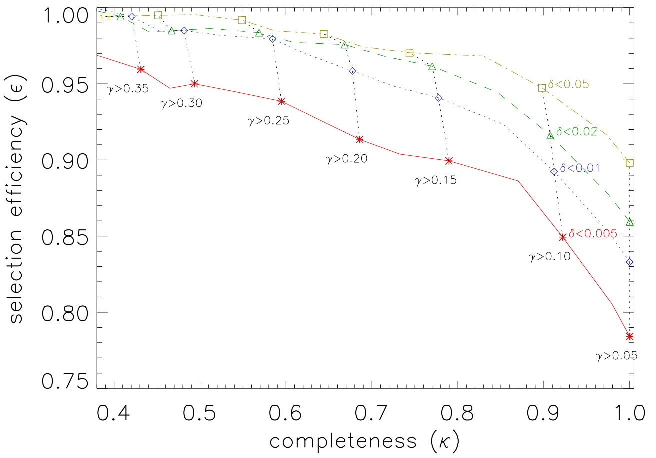

Figure 8. Selection efficiency versus completeness as a function of the threshold value used for the reliability parameter γ for redshift solutions with accuracy $\delta < 0.005$ (solid line), $\delta < 0.01$ (doted line), $\delta < 0.02$ (dashed line) and $\delta < 0.05$ (dot-dashed line).

In contrast, χ^2 values for ML solutions (lower panel in Figure 7) do not show an increase with δ. On the contrary, the higher χ^2 values occur preferably in sources with accurate redshifts, because these are usually the ones with higher SNR spectra. In other words: the χ^2 statistic correlates with the SNR of the spectrum, because at high SNR differences in the profile and strength of spectral features between spectrum and template are evident, while a very noisy spectrum blurs its features to the point that some of the templates can be considered an accurate model even at the wrong redshift. Therefore, the value of the absolute minimum in $\chi^2(z)$ cannot be used to identify the reliable ML solutions.

Since the MCPL algorithm offers higher redshift accuracy with a lower number of outliers, and also provides an indication on the reliability of the redshift solution, it can be considered superior to ML for this purpose. In the remaining sections, only results from MCPL will be discussed.

5.3 Selection efficiency and completeness

Let $N_g(D)$ be the number of sources with accuracy $\delta < D$, $N_s(G)$ the number of sources with $\gamma > G$, and $N_{sg}(D, G)$ the number of sources with $\delta < D$ and $\gamma > G$. The selection efficiency (ϵ) and the completeness (κ) are then defined by:

$$\epsilon(G, D) = \frac{N_{sg}(D, G)}{N_s(G)}, \qquad \kappa(G, D) = \frac{N_{sg}(D, G)}{N_g(D)} \tag{9}$$

As usual, there is a trade-off between completeness and selection efficiency, with either of them increasing only at the expense of the other. The relationship between ϵ and κ for a grid of values of D and G is shown in Figure 8.

For D values in the range 0.005–0.05, the completeness has a very small (but consistent) dependency on D that reflects the reduction in the average γ for higher values of δ. The dependency with G is much stronger due to the large number of sources with low γ values.

Efficiencies for $D = 0.01$, 0.02 and 0.05 converge rapidly to $\epsilon = 1$ with increasing γ, because there are almost no sources with high γ values and $\delta > 0.01$. Nevertheless, for $D = 0.005$ there is slower growth, since some sources with very high γ values have accuracies $0.005 < \delta < 0.01$.

5.4 Dependency with the MIR SED

Differences in the MIR SED of starburst-dominated versus AGN-dominated sources cause important variations in the average accuracy of the redshift solutions depending on the MIR SED type.

Normal and starburst galaxies usually have very prominent PAH bands that are easily identified even in low SNR spectra, and almost always obtain very accurate redshifts. On the other hand, sources dominated by AGN emission usually show a flat continuum with no high contrast features, and the redshift determination relies on broad and shallow silicate features (in emission or absorption) and/or unresolved emission lines, making it much harder to distinguish the peak in $Q_s(z)$ corresponding to the actual redshift of the source.

In Hernán-Caballero & Hatziminaoglou (2011) the ratio $r_{\rm PDR}$ of total PAH luminosity to the integrated restframe 5–15 μm luminosity is used to classify the ATLAS-IRS spectra into starburst-dominated (MIR_SB, $r_{\rm PDR} > 0.15$) and AGN-dominated (MIR_AGN, $r_{\rm PDR} < 0.15$). This is roughly equivalent to imposing a threshold EW ~0.2 μm in the equivalent width of the 6.2 μm or 11.3 μm PAH bands, which corresponds to roughly equal contributions from the starburst and AGN to the infrared luminosity of the galaxy (Hernán-Caballero et al. 2009). MIR_AGN sources are further separated into silicate emission (MIR_AGN1) and silicate absorption (MIR_AGN2) sources. Table 4 summarizes the accuracy and reliability statistics for these populations.

Sources dominated by star formation in their MIR spectra (MIR_SB) almost always obtain accurate redshifts. Among the 182 MIR_SB galaxies in the sample, MCPL solutions include only 2 outliers ($\delta > 0.02$), namely Murphy19 and NGC 4579. The optical redshift of the submillimeter galaxy Murphy19 (SDSS J123716.59+621643.9) is $z_{\rm spec} = 0.557$ (Wirth et al. 2004), but Murphy et al. (2009) give $z = 1.82$ based on the IRS spectrum. Although our solutions are consistent with the later ($z_{\rm MCPL} = 1.806$; $z_{\rm ML} = 1.795$), the second highest peak in $Q_s(z)$ is at $z = 0.5495$, indicating the optical redshift is confirmed with $\gtrsim$98% confidence (see §5.5). NGC 4579 (M 58) is a local spiral galaxy. The IRS spectrum contains emission from the LINER nucleus and its surroundings, and shows very intense H_2 lines combined with an unusual PAH spectrum (bright 11.3 μm PAH emission but very weak 6.2 and 7.7 μm bands). The lack of templates with significant H_2 emission is probably the cause of the wrong redshift solution for this source. In spite of that, the second highest peak in $Q_s(z)$ coincides with the optical redshift.

Sources classified as MIR_AGN have redshifts that are much less reliable compared to those for MIR_SB. The overall outlier rate is 22%, but there are strong variations in reliability among MIR_AGN subclasses: the fraction of outliers is 28% for MIR_AGN1 versus 8% for MIR_AGN2, and up to 40% for the MIR_AGN with no clear silicate emission or absorption. Nevertheless, if the outliers are removed, the accuracies for the remaining sources show very similar distributions in the MIR_SB, MIR_AGN1 and MIR_AGN2 subsamples (Figure 9).

Further insight into the importance of the PAH bands for the accuracy (or lack thereof) of the redshift solution can be obtained from Figure 10, which shows the strength of the PAH features, represented by $r_{\rm PDR}$, versus δ.

The subsample with $r_{\rm PDR} > 0.06$ includes by definition all the MIR_SB sources ($r_{\rm PDR} > 0.15$), the MIR composites ($r_{\rm PDR} \sim 0.15$), as well as some MIR_AGN with significant PAH emission. It comprises half of the total sample (242 sources) and has a 2% rate of outliers and a median accuracy $\tilde{\delta} = 9.6{\times}10^{-4}$.

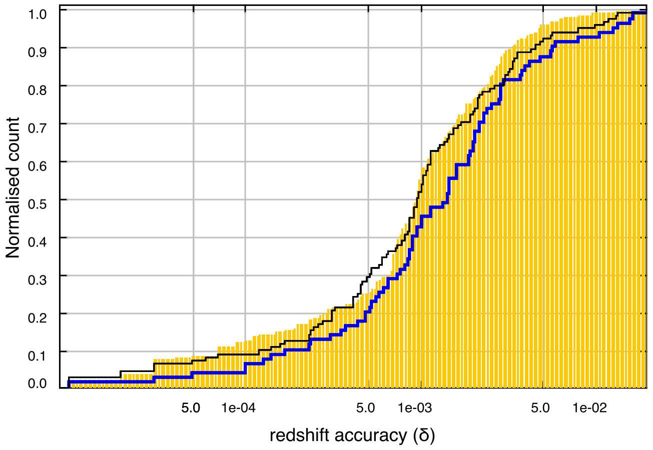

Figure 9. Normalized, cumulative distribution of δ values for MIR_SB (shaded area), MIR_AGN1 (thick solid line) and MIR_AGN2 (thin solid line) sources excluding outliers with δ 0.02.

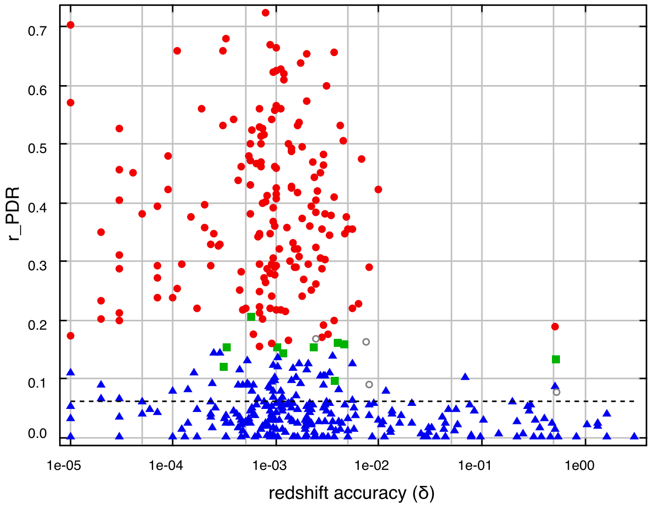

Figure 10. Ratio of total PAH luminosity to integrated 5–15 μm luminosity ($r_{\rm PDR}$) versus redshift accuracy of the MCPL solution for sources classified as MIR_SB (solid circles), MIR_AGN (triangles), composite sources (squares), and sources with no MIR classification (open circles). The dashed line marks $r_{\rm PDR} = 0.06$.

This demonstrates that detectable PAH emission is sufficient to obtain very accurate and reliable redshift estimates, even in high redshift sources with poor SNR spectra. But PAHs are not the only feature capable of providing an accurate estimate, since there are many accurate redshifts down to $r_{\rm PDR} \sim 0$.

Figure 11 shows the 9.7 μm apparent optical depth (a measurement of the strength of the silicate feature, see Hernán-Caballero & Hatziminaoglou (2011) for a discussion) versus δ for the sources with weak or undetected PAH bands ($r_{\rm PDR} < 0.06$). In this subsample, sources with silicate absorption ($\tau_{9.7} > 0$) are much more likely to obtain accurate redshifts than those with silicate emission (90% versus 70%, respectively, with $\delta < 0.02$), in spite of both populations having similar distributions of $r_{\rm PDR}$. This suggests that the silicate feature plays an important role in the redshift determination of sources with weak or no PAH emission. The diversity of shapes and lower contrast that the silicate feature

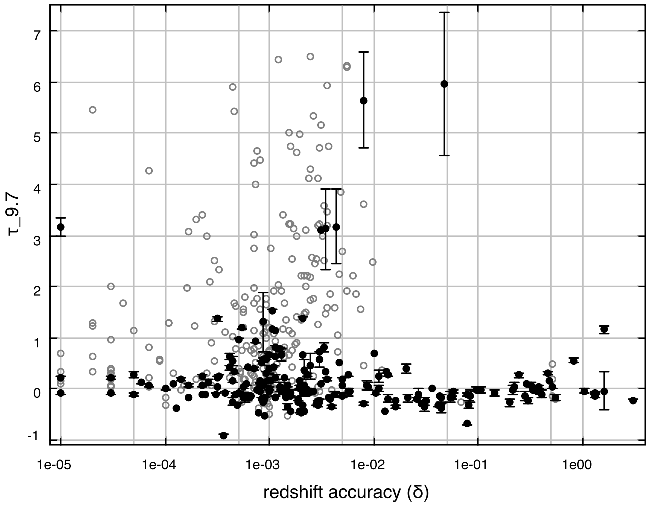

Figure 11. Optical depth at 9.7 μm ($\tau_{9.7}$) versus redshift accuracy. Solid symbols represent sources classified as MIR_AGN with very weak or absent PAH bands ($r_{\rm PDR} < 0.06$) while open symbols represent the rest of the sample. Negative (positive) $\tau_{9.7}$ values indicate silicate emission (absorption).

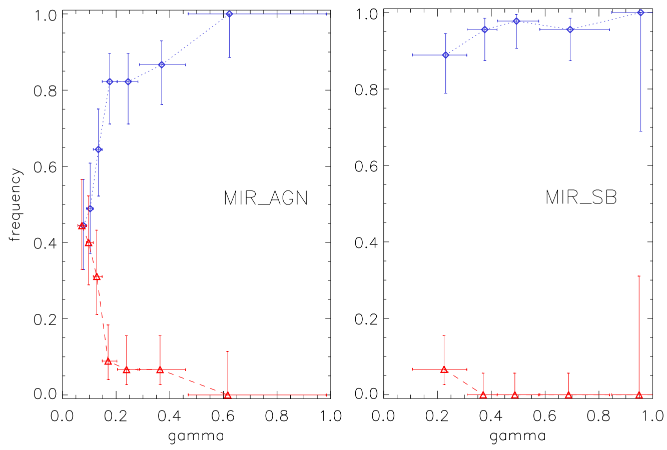

Figure 12. Frequency of highly accurate solutions ($\delta < 0.005$, blue diamonds) and outliers ($\delta > 0.02$, red triangles) as a function of γ for the sources classified as MIR_AGN (left panel) and MIR_SB (right panel). Each point represents a bin of γ containing 45 sources (except for the rightmost which contains the remainder). Horizontal bars represent the γ range covered by each bin, while vertical error bars represent the 90% confidence intervals calculated using the Wilson score formula for binomial distributions.

presents when it appears in emission might be at least in part responsible for the decreased efficiency in these sources.

Albeit the rate of outliers is much higher in MIR_AGN compared to MIR_SB sources, the reliability of redshift estimates within a given γ interval is largely independent on the MIR classification. Figure 12 shows the frequencies of highly accurate solutions ($\delta < 0.005$) and outliers ($\delta > 0.02$) as a function of γ for the MIR_AGN and MIR_SB populations separately. They are found to agree within their 90% confidence limits.

These confidence intervals can be used to put a lower limit on the probability of the redshift solution for a given source having accuracy better than some predefined value, or an upper limit on the probability of being an outlier. A more detailed model of such probabilities based on a much larger sample of MIR spectra from the CASSIS database is under development, and will be presented elsewhere (Hernán-Caballero et al., in preparation).

5.5 Redshift degeneracies

There are 69 outliers ($\delta > 0.02$) in the sample, 40 of them with catastrophic errors ($\delta > 0.1$) in their redshift estimates.

Typical values of γ for the outliers are low, with 60% of them below 0.15 (compared to just 20% in the whole sample). They show multiple secondary peaks in the $Q_s(z)$ distribution, with highest to second-highest ratios (R) in the range $1 < R < 3$, and in 90% of cases verifying $R < 2$ (compared to only 36% in the sources with $\delta < 0.02$). This suggests that most of these sources have degeneracy issues, and somehow spurious solutions obtain a $Q_s(z)$ value higher than the peak for the actual redshift of the source.

Another possibility that deserves consideration is a wrong or inaccurate optical redshift. One way to rule out an error in the optical redshift is to search for a secondary peak in $Q_s(z)$ that matches the $z_{\rm spec}$ value. If a significant peak is found very close to it, the optical redshift can be confirmed with high probability. On the other hand, the lack of a nearby secondary peak does not imply that $z_{\rm spec}$ is wrong, since spectra with very exotic MIR SEDs, strong artefacts or very low signal to noise ratios could produce a very weak peak at the actual redshift that passes unnoticed.

To find out whether there are secondary solutions backing up the $z_{\rm spec}$ value for the 69 outliers, a routine finds all the peaks in the $Q_s(z)$ distribution that verify $\gamma > 0.01$, and sorts them by their γ value. 48 outliers show at least one such secondary peak within $\delta < 0.02$ of the $z_{\rm spec}$ value. They are all listed in Table 5.

Since the redshift search range is very wide compared to the typical δ of these solutions, the probability of them occurring that close to $z_{\rm spec}$ fortuitously is low. If spurious peaks in $Q_s(z)$ are assumed to be randomly distributed in the redshift search range, the probability for a spurious solution obtaining accuracy δ or better is:

$$P = \frac{2\delta}{\ln(1 + z_{max})} \tag{10}$$

where z_{max} is the upper limit of the redshift search range for that particular source.

For a $Q_s(z)$ distribution with several spurious peaks, the probability that at least one of the n highest peaks is within δ of $z_{\rm spec}$ just by chance is then:

$$P_r(n) = 1 - (1 - P)^n \tag{11}$$

Probabilities P_r for the secondary solutions of these 48 outliers are listed in the last column of Table 5. 34 of them have $P_r <$ 5%, thus confirming the $z_{\rm spec}$ value with confidence $\gtrsim$ 95%, while the other 14 have $0.05 < P_r < 0.25$, and some of them could be just random alignments.

5.6 Nature of outliers

Individualised inspection of outliers reveals a large number of radiogalaxies and radio-loud quasars among them. The remainder are high redshift sources (mostly quasars) with poor SNR spectra.

Among the 21 outliers with no significant ($\gamma > 0.01$) secondary solutions within $\delta < 0.02$ of $z_{\rm spec}$ there are 4 local radiogalaxies (3C 83.1, 3C 465, 3C 371, and 3C 390.3) and two intermediate redshift radio-loud quasars (PG 2251+113 and 3C 295). The spectra of these 6 sources have high SNR, but are very different from each other. 3C 390.3 and PG 2251+113 show continuum emission peaking at ~ 20 μm, a wide silicate emission feature and strong emission in the lines [NeII] 12.81 μm, [NeIII]15.55 μm, and [OIV] 25.91 μm. 3C 83.1 and 3C 465 have a very weak MIR continuum dominated at $\lambda < 10$ μm by the Rayleigh-Jeans tail of stellar emission, and also show clear neon lines. 3C 371 is a flat spectrum radio source dominated by synchrotron emission in the MIR with no significant features. Finally, 3C 295 has a steep continuum lacking significant features and seems to have stitching issues in the LL2 module.

The redshift misidentification in all but the last two sources seems not to arise from a lack of spectral features capable of providing an accurate redshift estimate, but rather, from an inadequate representation of these features in the set of templates used.

Another object, SWIRE J104354.82+585902.4, has conflicting optical redshift estimates: Trouille et al. (2008) give z = 0.35, while Weedman et al. (2006) give $z = 1.14 \pm 0.2$, much closer to the value 1.079 found here.

The remaining 14 sources are high redshift ($z_{\rm spec} > 1$) quasars and infrared galaxies with very low SNR spectra.

6 CONCLUSIONS

In this work we apply a new SED-fitting algorithm to the problem of measuring redshifts in MIR low resolution spectra. The algorithm is based on the same SED-fitting technique applied to broad-band photometric redshifts, but with some important modifications that largely increase its efficiency with MIR spectra. Namely: a wavelength dependent scaling factor for the template, which adds flexibility to the fit, and a novel algorithm for filtering and combining prospective redshift solutions, dubbed “Maximum Combined Pseudo-likelihood” (MCPL).

The efficiency of MCPL is compared to regular Maximum likelihood (ML) using a sample of 491 *Spitzer*/IRS spectra for sources with accurate optical or NIR spectroscopic redshifts. The spectral templates used are obtained from *Spitzer*/IRS, *AKARI*/IRC and *ISO*/SWS spectroscopy of low redshift galaxies, as well as composite templates of *Spitzer*/IRS spectra of higher redshift sources.

MCPL offers superior performance compared to ML both in terms of the number of highly accurate ($\Delta(z)/(1+z) < 0.005$) redshift solutions (78% versus 68% of the sample) and in the number of outliers ($\Delta(z)/(1+z) > 0.02$; MCPL: 14%, ML: 22%). Excluding outliers, the dispersion in the redshift errors is also lower for MCPL: $\sigma = 0.0033$ (versus 0.0045 for ML).

The reduced χ^2 statistic that determines the goodness of fit, often used to evaluate the reliability of the redshift solution, is found to correlate strongly with the SNR of the spectrum. High SNR spectra obtain higher χ^2 values, indicating the differences between spectrum and template are more evident in them compared to low SNR spectra. Nevertheless, the accuracy of the ML redshift solution does not correlate with χ^2, and thus cannot be directly used to estimate the confidence level of the redshift solution. On the other hand, the normalised combined pseudo-likelihood (γ) offers a good indication on the reliability of the MCPL solution for individual spectra, with the median accuracy and rate of outliers both monotonically decreasing with increasing γ.

The fraction of accurate redshift solutions is much higher among sources classified as starbursts by their MIR emission compared to those classified as AGN (2% versus 21% rate of outliers), thanks to the high contrast of the PAH emission bands, which are easily identified even in very low SNR spectra. The rate of outliers is also larger in AGN with the 10 μm silicate feature in emission compared to those in absorption. Nevertheless, for any given γ range the accuracy of MCPL redshifts is largely independent of the MIR SED type.

Finally, we find that most outliers are radiogalaxies, radio-loud quasars, or high redshift sources (mostly quasars) with very poor SNR. About 2/3 of outliers show secondary MCPL solutions at the optical redshift. This indicates that degeneracy issues favoured spurious solutions in the selection process. This could be mitigated with templates that reproduce with greater fidelity the properties of these sources, in particular, radiogalaxies.

ACKNOWLEDGEMENTS

This work is based on observations made with the *Spitzer Space Telescope*, which is operated by the Jet Propulsion Laboratory, Caltech under NASA contract 1407. The Cornell Atlas of Spitzer/IRS Sources (CASSIS) is a product of the Infrared Science Center at Cornell University, supported by NASA and JPL. We wish to thank A. Alonso-Herrero, E. Hatziminaoglou, and the anonymous referee for useful comments that helped to improve this paper. A.H.-C. is funded by the Universidad de Cantabria Augusto González Linares program.

REFERENCES

Abramo L. R. et al., 2012, MNRAS, 423, 3251
Avni Y., 1976, ApJ, 210, 642
Assef R. J. et al., 2008, ApJ, 676, 286.
Babbedge T., et al. 2004, MNRAS, 353, 654
Baum W. A., 1962, in IAU Symp. Ser. 15, Problems of Extra-Galactic Research, ed. G.C. McVittie (Cambridge: Cambridge Univ. Press), 390
Benítez N., et al. 2009, ApJ, 692, 5
Benítez N., 2000, ApJ, 536, 571
Bolzonella M., Miralles J. M., Pell R., 2000, A&A 363, 476
Brunner R. J., Connolly A. J., Szalay A. S., & Bershady M. A. 1997, ApJ, 482, 21
Brodwin M. et al., 2006, ApJ, 651, 791
Bruzual G. & Charlot S., 1993, ApJ, 405, 538
Bruzual G., Charlot S., 2003, MNRAS, 344, 1000
Carliles S., Budavári T., Heinis S., Priebe C., Szalay A. S., 2010, ApJ, 712, 511
Coleman G. D., Wu C. C., Weedman D. W., 1980, ApJS, 43, 393
Collister A., Lahav O., 2004, PASP, 116, 345
Connolly A. J., Csabai I., Szalay A. S., Koo D. C., Kron R. G., & Munn J. A. 1995, AJ, 110, 2655
Farrah D., Weedman D., Lonsdale C. J., Polletta M., Rowan-Robinson M., Houck J., Smith H. E. 2009, ApJ, 696, 2044
Feldmann R. et al., 2006, MNRAS, 372, 565
Fernández-Soto A., Lanzetta K. M., Yahil A., 1999, ApJ, 513, 34
Goicoechea J. R., Roelfsema P. R., Jellema W., Swinyard B. M., 2011, IAUS, 280, 179
Gwyn S. D. J., Hartwick F. D. A., 1996, ApJ, 468, 77
Hatziminaoglou E., Mathez G., Pelló R., 2000, A&A, 359, 9
Hernán-Caballero A. & Hatziminaoglou E., 2011, MNRAS, 414, 500

Hernán-Caballero A. et al., 2009, MNRAS, 395, 1695
Houck J.R., et al. 2004, SPIE, 5487, 62
Houck J.R., Weedman D. W., Le Floc'h E., Hao L., 2007, ApJ, 671, 323
Ilbert O. et al., 2006, A&A, 457, 841
Imanishi M., Nakagawa T., Shirahata M., Ohyama Y., Onaka T., 2010, ApJ, 721, 1233
Koo D. C. 1985, AJ, 90, 418
Lanzetta K. M., Yahil A., & Fernandez-Soto A. 1996, Nature, 381, 759
Le Borgne D. & Rocca-Volmerange B., 2002, A&A, 386, 446
Lebouteiller V., Barry D.J., Spoon H.W.W., Bernard-Salas J., Sloan G.C., Houck J.R., & Weedman D., 2011, ApJS, 196, 8
Matute I., et al. 2012, A&A, 542, 20
Murakami H., et al. 2007, PASJ, 59, 369
Murphy E. J. et al., 2009, ApJ, 698, 1380
Negrello M. et al., 2009, MNRAS, 394, 375
Onaka T. et al., 2007, PASJ, 59, 401
Oyaizu H., Lima M., Cunha C. E., Lin H., Frieman J., 2008, ApJ, 689, 709
Pope A. et al., 2008, ApJ, 689, 127
Pirzkal N. et al., 2004, ApJS, 154, 501
Press W. H., Teukolsky S. A., Vetterling W. T., Flannery B. P. 1992, Numerical Recipes in C: The Art of Scientific Computing (2nd ed.; Cambridge: University Press)
Richards G. T. et al., 2001, AJ, 122, 1151
Rowan-Robinson M. et al., 2008, MNRAS, 386, 697
Sawicki M. J., Lin H., Yee H. K. C., 1997, AJ, 113, 1
Silva L., Granato G. L., Bressan A. & Danese L., 1998, ApJ, 509, 103
Trouille L., Barger A. J., Cowie L. L., Yang Y., Mushotzky R. F, ApJS, 179, 1
Wada T. & Kataza H., 2010, SPIE, 7731, 23
Wadadekar Y., 2005, PASP, 117, 79
Wang Y., Bahcall N., & Turner E. L. 1998, AJ, 116, 2081
Weedman D. W. et al., 2006, ApJ, 653, 101
Weedman D. W. et al., 2009, ApJ, 693, 370
Wirth G. D. et al., 2004, AJ, 127, 3121
Wright G. S. et al., 2008, SPIE, 7010, 27
Yan L. et al., 2007, ApJ, 658, 778

Table 1. Results for individual sources

source ID (1)	RA (J2000.0) (2)	Dec (J2000.0) (3)	$z_{\rm spec}$ (4)	$z_{\rm MCPL}$ (5)	$z_{\rm ML}$ (6)	γ (7)	R (8)	$\log \mathcal{N}$ (9)	$\log \chi^2_{\rm ML}$ (10)	MIRclass (11)
UGC 00006	00:03:09.60	+21:57:37.0	0.0220	0.0222	0.0202	0.62	9.83	5.30	2.79	MIR_SB
[HB89] 0003+199	00:06:19.50	+20:12:10.0	0.0260	0.0284	0.0284	0.20	2.19	3.75	0.20	MIR_AGN1
2MASX J00070361+1554240	00:07:03.60	+15:54:24.0	0.1140	0.1118	1.5595	0.15	1.44	4.48	1.64	MIR_AGNx
III Zw 002	00:10:30.80	+10:58:13.0	0.0898	0.0898	0.0876	0.17	2.45	4.79	1.99	MIR_AGN1
NGC 0017	00:11:06.50	-12:06:26.0	0.0196	0.0202	0.0202	0.52	19.96	4.11	1.73	MIR_SB
2MASX J00114330-0722073	00:11:43.30	-07:22:07.0	0.1180	0.1185	0.1185	0.82	17.71	4.99	2.02	MIR_SB
2MASX J00212652-0839261	00:21:26.50	-08:39:26.0	0.1280	0.1320	0.1320	0.46	9.23	4.97	2.48	MIR_AGN2
LBQS 0018-0220	00:21:27.30	-02:03:33.0	2.5960	0.8183	2.5958	0.11	1.80	3.60	0.31	MIR_AGN
2MASX J00215355-7910077	00:21:57.00	-79:10:14.0	0.0728	0.0304	0.0304	0.13	1.47	4.62	0.92	MIR_AGN
PG 0026+129	00:29:13.60	+13:16:03.0	0.1420	0.1388	0.2585	0.13	1.06	4.16	1.22	MIR_AGN1
ELAISC15 J002925-434917	00:29:25.82	-43:49:19.5	3.0940	3.0867	3.0867	0.10	1.75	3.14	-0.59	MIR_AGN
SWIRE4 J002959.22-434835.1	00:29:59.21	-43:48:35.3	2.0390	2.1324	2.1324	0.06	1.03	3.82	0.05	MIR_AGN1
[HB89] 0027-289 NED02	00:30:04.20	-28:42:25.0	0.2781	0.2840	0.2840	0.20	2.19	4.19	1.24	MIR_AGN2
ELAISC15 J003014-430332	00:30:15.00	-43:03:33.7	1.6540	1.3770	2.3460	0.09	1.33	3.17	-0.65	MIR_AGNx
GALEX 2533910445613399575	00:32:13.15	-43:45:53.5	1.7070	1.9677	1.9677	0.12	1.24	3.99	0.06	MIR_AGNx
ESIS J003234.34-431937.8	00:32:34.34	-43:19:37.9	1.6370	1.0624	1.0175	0.12	1.69	2.89	-0.70	MIR_AGNx
ESIS J003408.93-431012.4	00:34:08.93	-43:10:12.3	1.0650	1.0624	1.0624	0.10	1.38	3.08	-0.50	MIR_AGNx
ESIS J003640.40-433926.3	00:36:40.41	-43:39:26.4	1.1810	1.1638	1.1638	0.07	1.17	3.32	-0.34	MIR_AGN1
3C 015	00:37:04.10	-01:09:08.1	0.0730	3.3134	3.3134	0.07	1.09	3.90	0.99	MIR_AGN1
ELAISC15 J003715-423515	00:37:15.65	-42:35:14.1	2.1900	1.3114	2.4826	0.08	1.33	3.71	-0.06	MIR_AGN1
ESIS J003814.10-433314.9	00:38:14.12	-43:33:14.9	1.4000	1.3865	1.6908	0.08	1.05	3.12	-0.70	MIR_AGN1
ESIS J003829.91-434454.3	00:38:29.93	-43:44:54.2	1.5670	1.5595	1.5595	0.13	1.76	3.98	-0.06	MIR_AGN1
ESO 012- G 021	00:40:47.80	-79:14:27.0	0.0328	0.0325	0.0325	0.48	5.11	3.71	0.69	MIR_SB
APMUKS(BJ) B003833.18-442916.3	00:40:55.65	-44:12:49.5	1.3800	0.6618	1.3961	0.07	1.05	3.68	-0.02	MIR_AGN1
IRAS 00397-1312	00:42:15.50	-12:56:03.0	0.2610	0.2585	0.2585	0.48	10.50	5.00	3.19	MIR_AGN2
2MASX J00480675-2848187	00:48:06.80	-28:48:19.0	0.1100	0.1118	0.1074	0.38	4.72	4.17	2.04	MIR_SB
NGC 0262	00:48:47.10	+31:57:25.0	0.0150	0.0161	0.0161	0.63	7.79	3.91	0.52	MIR_AGN2
SDSS J005009.81-003900.5	00:50:09.81	-00:39:00.6	0.7280	0.7296	0.7296	0.27	3.30	3.86	0.98	MIR_AGN2
IRAS 00482-2720	00:50:40.30	-27:04:41.0	0.1290	0.1275	0.1275	0.50	6.84	4.49	1.43	MIR_SB
2MASX J00505570+2933281	00:50:55.70	+29:33:28.0	0.1360	0.1365	0.1365	0.17	1.17	4.47	0.90	MIR_AGN2
UGC 00545	00:53:34.90	+12:41:36.0	0.0610	0.0618	0.0618	0.28	1.90	5.39	2.83	MIR_AGN1
2MASX J00535615-7038045	00:53:56.20	-70:38:03.0	0.0689	0.0661	0.0661	0.10	1.59	4.65	1.44	MIR_AGN
PG 0052+251	00:54:52.10	+25:25:38.0	0.1550	0.1252	0.1252	0.16	1.61	3.73	0.33	MIR_AGN1
SDSS J005621.72+003235.6	00:56:21.72	+00:32:35.8	0.4840	0.4887	0.4769	0.25	1.07	3.31	0.81	MIR_SB
UGC 00595	00:57:34.90	-01:23:27.9	0.0450	0.3826	3.3481	0.09	1.09	3.34	0.14	MIR_AGN2
ESO 541-IG 012	01:02:17.50	-19:40:09.0	0.0565	0.0492	0.0492	0.09	1.64	4.31	0.29	MIR_AGN
IRAS 01003-2238	01:02:50.00	-22:21:57.0	0.1180	0.1163	0.1163	0.24	2.05	5.22	2.97	MIR_AGN2
NGC 0383	01:07:24.90	+32:24:45.2	0.0170	0.0161	0.0161	0.22	2.36	4.10	1.73	MIR_SB
2MASSi J0108351+214818	01:08:35.10	+21:48:18.0	0.2850	0.2840	1.1552	0.11	1.19	4.54	1.13	MIR_AGN2
NGC 0424	01:11:27.60	-38:05:00.0	0.0120	0.0060	0.0060	0.37	2.18	4.25	0.98	MIR_AGN1
2MASX J01190760-0829095	01:19:07.70	-08:29:10.0	0.1180	0.1118	0.1118	0.40	1.39	4.08	1.65	MIR_SB
CGCG 502-027	01:19:35.00	+32:10:50.0	0.0602	0.0597	0.0597	0.23	2.52	3.75	0.76	MIR_AGN2
IRAS 01199-2307	01:22:20.90	-22:52:07.0	0.1560	0.1525	0.1525	0.62	23.86	4.03	1.12	MIR_SB
SDSS J012341.46+004435.9	01:23:41.47	+00:44:35.9	0.3990	2.2602	0.4105	0.08	1.21	3.67	0.07	MIR_AGN1
FAIRALL 0009	01:23:45.80	-58:48:20.0	0.0460	0.0429	0.0429	0.42	3.81	5.16	2.16	MIR_AGN1
NGC 0526A	01:23:54.40	-35:03:56.0	0.0190	0.0182	0.0182	0.52	3.73	4.26	1.54	MIR_AGN1
NGC 0513	01:24:26.80	+33:47:58.0	0.0195	0.0202	0.0182	0.30	3.17	3.62	0.67	MIR_SB
NGC 0520	01:24:35.07	+03:47:32.7	0.0071	0.0080	0.0080	0.80	—	4.71	2.79	MIR_SB
IRAS 01298-0744	01:32:21.40	-07:29:08.0	0.1360	0.1388	0.1388	0.71	9.55	4.88	2.24	MIR_SB
3C 048	01:37:41.30	+33:09:35.0	0.3670	0.3688	0.3743	0.10	1.08	4.37	1.46	MIR_AGN1
IRAS 01355-1814	01:37:57.40	-17:59:21.0	0.1920	0.1876	0.1876	0.63	17.72	3.84	0.89	MIR_SB
NGC 0660	01:43:02.35	+13:38:44.4	0.0029	0.0040	-0.0020	0.57	—	4.76	3.00	MIR_SB
2MASX J01500266-0725482	01:50:02.70	-07:25:48.0	0.0180	0.0876	0.0876	0.24	1.04	3.87	0.69	MIR_AGN1
2MASX J01515140-1830464	01:51:51.40	-18:30:46.0	0.1580	0.1572	0.1525	0.42	7.86	3.83	1.32	MIR_SB
UGC 01395	01:55:22.00	+06:36:43.0	0.0170	0.0182	0.0182	0.26	2.50	3.75	0.45	MIR_AGN2
2MASSi J0157210+171248	01:57:21.00	+17:12:48.0	0.2130	0.2140	0.2140	0.31	3.02	4.24	1.31	MIR_AGN2
2MASX J01591372-2924356	01:59:13.80	-29:24:35.0	0.1410	0.1411	0.1411	0.77	30.47	4.06	1.15	MIR_SB

Table 1 (cont'd)

source ID (1)	RA (J2000.0) (2)	Dec (J2000.0) (3)	$z_{\rm spec}$ (4)	$z_{\rm MCPL}$ (5)	$z_{\rm ML}$ (6)	γ (7)	R (8)	$\log \mathcal{N}$ (9)	$\log \chi^2_{\rm ML}$ (10)	MIRclass (11)
2MASX J02042730-2049413	02:04:27.30	-20:49:41.0	0.1160	0.1230	0.1230	0.34	2.09	4.84	1.85	MIR_SB
IRAS 02054+0835	02:08:06.80	+08:50:02.0	0.3450	0.3525	0.3525	0.12	1.20	4.80	1.94	MIR_AGN1
2MASX J02215058+1327409	02:21:50.60	+13:27:41.0	0.1400	0.1549	0.1549	0.20	1.49	4.63	1.12	MIR_AGN2
UGC 01841	02:23:11.40	+42:59:31.4	0.0212	0.0222	0.0222	0.13	1.07	3.89	0.64	MIR_AGN2
MRK 1034 NED01	02:23:18.90	+32:11:18.0	0.0336	0.0346	0.0346	0.37	5.85	4.80	2.54	MIR_SB
MRK 1034 NED02	02:23:22.00	+32:11:49.0	0.0337	0.0325	0.0325	0.21	3.38	4.28	0.86	MIR_SB
ESO 545- G 013	02:24:40.20	-19:08:27.0	0.0337	0.0471	0.0534	0.14	2.37	4.14	0.51	MIR_SB
NGC 0931	02:28:14.50	+31:18:42.0	0.0170	0.0182	0.0182	0.38	4.76	4.01	0.54	MIR_AGN1
HE 0230-2130	02:32:33.10	-21:17:26.0	2.1620	2.1575	2.1575	0.07	1.06	3.51	0.12	MIR_AGN
2MASX J02343065+2438353	02:34:30.60	+24:38:35.0	0.3100	0.3125	0.4505	0.18	1.05	3.93	0.77	MIR_AGN1
NGC 1056	02:42:48.30	+28:34:27.0	0.0050	0.0060	0.0060	0.51	3.28	3.81	1.44	MIR_SB
2MASX J02434617+0406377	02:43:46.10	+04:06:37.0	0.1440	0.1434	0.1434	0.60	9.93	4.18	1.53	MIR_SB
NGC 1097	02:46:19.08	-30:16:28.0	0.0040	0.0020	0.0020	0.77	8.14	4.58	2.77	MIR_SB
IRAS 02480-3745	02:50:01.70	-37:32:45.0	0.1650	0.1572	0.1572	0.51	4.09	3.92	1.32	MIR_SB
NGC 1125	02:51:40.30	-16:39:04.0	0.0110	0.0100	0.0100	0.63	6.82	3.86	0.58	MIR_SB
NGC 1142	02:55:12.20	-00:11:01.0	0.0290	0.0304	0.0304	0.57	25.87	3.37	0.51	MIR_SB
UGC 02456	02:59:58.60	+36:49:14.0	0.0120	0.0121	0.0100	0.72	18.02	5.61	3.35	MIR_SB
MCG -02-08-039	03:00:30.60	-11:24:57.0	0.0290	0.0304	0.0304	0.53	5.49	3.74	0.78	MIR_AGNx
CFRS 03.0346	03:02:27.73	+00:06:53.5	1.4080	1.4057	1.4057	0.20	4.15	2.61	-0.87	MIR_SB
3C 076.1	03:03:15.00	+16:26:19.0	0.0324	0.8812	1.3913	0.09	1.54	3.22	0.19	MIR_AGN2
NGC 1194	03:03:49.10	-01:06:13.0	0.0140	0.0161	0.0182	0.21	1.33	3.88	1.17	MIR_AGN2
NGC 1222	03:08:56.74	-02:57:18.5	0.0076	0.0080	0.0080	0.70	11.89	4.54	1.80	MIR_SB
3C 079	03:10:00.10	+17:05:58.0	0.2560	0.2560	0.2585	0.13	1.02	4.34	1.11	MIR_AGN2
NGC 1241	03:11:14.60	-08:55:20.0	0.0140	0.0141	0.0141	0.38	9.21	3.59	0.61	MIR_SB
NGC 1265	03:18:15.80	+41:51:27.8	0.0251	0.5464	0.5464	0.36	1.14	3.92	0.69	MIR_AGN2
NGC 1275	03:19:48.10	+41:30:42.0	0.0170	0.0161	0.0161	0.41	3.32	4.66	1.93	MIR_AGN1
SDSS J032322.86-075615.2	03:23:22.90	-07:56:15.0	0.1664	0.1665	0.1688	0.39	6.22	4.62	2.06	MIR_SB
NGC 1320	03:24:48.70	-03:02:32.0	0.0090	0.0100	0.0080	0.39	5.03	4.01	0.64	MIR_AGN2
MRK 0609	03:25:25.30	-06:08:38.0	0.0340	0.0346	0.0346	0.45	6.28	4.18	1.79	MIR_SB
2MASX J03274981+1616594	03:27:49.80	+16:17:00.0	0.1290	0.1320	0.0942	0.28	1.80	4.59	2.15	MIR_SB
NGC 1365	03:33:36.37	-36:08:25.5	0.0054	0.0060	0.0060	0.31	3.63	5.11	3.12	MIR_SB
NGC 1386	03:36:46.20	-35:59:57.0	0.0030	0.0020	0.0020	0.47	5.26	4.08	1.23	MIR_COMP
IC 0342	03:46:48.51	+68:05:46.0	0.0010	0.0020	0.0020	1.00	—	4.83	3.43	MIR_SB
2MASX J03474022+0105143	03:47:40.20	+01:05:14.0	0.0310	0.0202	0.0202	0.29	1.17	5.11	2.36	MIR_AGN1
SDSS J035442.18+003703.0	03:54:42.20	+00:37:03.0	0.1520	0.1456	0.1456	0.59	14.01	4.02	1.35	MIR_SB
4C +37.11	04:05:49.20	+38:03:32.0	0.0550	0.0555	0.0555	0.11	1.63	3.62	0.66	MIR_AGN2
IRAS 04074-2801	04:09:30.40	-27:53:44.0	0.1530	0.1549	0.1549	0.69	24.94	4.12	1.41	MIR_SB
2MASX J04121945-2830252	04:12:19.40	-28:30:25.0	0.1180	0.1185	0.1185	0.35	5.25	5.20	2.35	MIR_AGN2
SMM J041327.2+102743	04:13:27.26	+10:27:40.5	2.8370	2.8334	2.8334	0.07	1.10	3.03	-0.13	MIR_AGN
3C 109	04:13:40.40	+11:12:14.0	0.3060	0.3073	0.3073	0.22	2.11	4.79	1.42	MIR_AGNx
NGC 1566	04:20:00.40	-54:56:16.0	0.0050	0.0040	0.0040	0.41	3.20	4.34	2.08	MIR_SB
IRAS 04313-1649	04:33:37.00	-16:43:32.0	0.2680	0.2611	0.2611	0.38	5.51	3.85	1.05	MIR_AGN2
NGC 1614	04:33:59.85	-08:34:44.0	0.0149	0.0141	0.0121	0.61	9.60	5.71	3.82	MIR_SB
2MASX J04405494-0822221	04:40:54.90	-08:22:22.0	0.0150	0.0161	0.0284	0.15	1.25	4.08	1.21	MIR_AGN2
NGC 1667	04:48:37.10	-06:19:12.0	0.0150	0.0161	0.0161	0.52	6.04	3.71	1.19	MIR_SB
WEIN 045	04:49:09.00	+45:00:39.2	0.0208	0.0222	0.0222	0.11	1.03	3.83	0.58	MIR_AGN2
ESO 033- G 002	04:55:58.90	-75:32:28.0	0.0181	0.0182	0.0182	0.26	1.87	3.81	0.70	MIR_AGN2
IRAS 05020-2941	05:04:00.70	-29:36:55.0	0.1540	0.1549	0.1549	0.63	10.22	4.78	1.93	MIR_SB
ESO 362- G 018	05:19:35.80	-32:39:28.0	0.0120	0.0121	0.0121	0.35	4.14	3.80	0.40	MIR_SB
PICTOR A	05:19:49.70	-45:46:44.0	0.0340	0.0040	0.0040	0.15	1.05	4.79	2.63	MIR_AGN1
2MASX J05210136-2521450	05:21:01.50	-25:21:45.0	0.0430	0.0408	0.2943	0.50	1.57	5.72	3.82	MIR_AGN2
NGC 2110	05:52:11.40	-07:27:22.0	0.0080	0.0080	0.0080	0.16	1.76	4.76	2.55	MIR_AGN1
UGC 03426	06:15:36.30	+71:02:15.0	0.0130	0.0121	0.0121	0.67	4.64	4.64	2.29	MIR_AGN2
NGC 2146	06:18:37.71	+78:21:25.3	0.0039	0.0040	0.0000	0.59	—	4.94	3.38	MIR_SB
NGC 2273	06:50:08.60	+60:50:45.0	0.0060	0.0060	0.0040	0.60	3.66	5.46	3.01	MIR_SB
IC 0450	06:52:12.20	+74:25:37.0	0.0190	0.0182	0.0202	0.49	4.13	3.89	0.93	MIR_AGN2
ESO 428- G 014	07:16:31.20	-29:19:29.0	0.0060	0.0060	0.0060	0.45	2.89	4.42	1.88	MIR_AGN2

Table 1 (cont'd)

source ID (1)	RA (J2000.0) (2)	Dec (J2000.0) (3)	$z_{\rm spec}$ (4)	$z_{\rm MCPL}$ (5)	$z_{\rm ML}$ (6)	γ (7)	R (8)	$\log \mathscr{N}$ (9)	$\log \chi^2_{\rm ML}$ (10)	MIRclass (11)
MRK 0009	07:36:57.00	+58:46:13.0	0.0399	0.0408	0.0429	0.27	2.59	3.80	0.32	MIR_AGNx
UGC 03973	07:42:32.80	+49:48:35.0	0.0220	0.0222	0.0243	0.25	2.76	3.95	0.57	MIR_AGN2
NGC 2484	07:58:28.10	+37:47:11.8	0.0408	0.4332	2.6102	0.08	1.12	3.61	0.37	MIR_AGNx
IRAS 07598+6508	08:04:33.10	+64:59:49.0	0.1483	0.1479	0.1479	0.26	1.24	4.47	1.72	MIR_AGN1
UGC 04229	08:07:41.00	+39:00:15.0	0.0230	0.0222	0.0222	0.21	1.31	5.03	2.66	MIR_SB
PG 0804+761	08:10:58.60	+76:02:42.0	0.1000	0.1140	0.1140	0.21	1.69	4.24	1.16	MIR_AGN1
2MASSi J0812004+402815	08:12:00.54	+40:28:13.0	1.7950	1.8174	1.8174	0.09	1.16	3.75	-0.03	MIR_AGN
[KMT2006] J081253.12+401859.	08:12:53.09	+40:18:59.9	0.5510	0.5495	0.5495	0.10	2.18	3.07	-0.27	MIR_AGN2
SDSS J081507.42+430427.1	08:15:07.42	+43:04:27.2	0.5097	0.5097	0.4828	0.11	1.49	3.45	1.40	MIR_AGN2
SDSS J082312.61+275139.8	08:23:12.60	+27:51:40.0	0.1680	0.1641	0.1641	0.46	11.47	4.04	1.52	MIR_SB
NGC 2622	08:38:10.90	+24:53:43.0	0.0290	0.0284	0.0284	0.57	6.06	4.60	1.71	MIR_AGN2
NGC 2623	08:38:24.08	+25:45:16.9	0.0185	0.0161	0.0161	0.69	—	5.49	3.26	MIR_SB
4C +29.31	08:43:09.90	+29:44:04.9	0.3980	1.8457	0.4361	0.07	1.05	3.74	0.21	MIR_AGN1
NGC 2639	08:43:38.10	+50:12:20.0	0.0110	0.0100	0.0100	0.28	3.98	3.41	0.46	MIR_SB
VII Zw 244	08:44:45.20	+76:53:09.0	0.1310	0.1320	0.1320	0.15	2.20	4.88	1.08	MIR_AGN1
2MASSi J0845387+342043	08:45:38.70	+34:20:44.0	0.1490	0.1434	0.1434	0.16	1.17	3.82	-0.00	MIR_AGN2
SDSS J085018.31+180200.9	08:50:18.30	+18:02:01.0	0.1454	0.1343	0.1343	0.28	1.97	3.76	1.67	MIR_SB
IRAS 08572+3915	09:00:25.40	+39:03:54.0	0.0580	0.0618	0.0618	0.38	2.40	5.58	4.05	MIR_COMP
IRAS 08592+5248	09:02:47.50	+52:36:30.0	0.1580	0.1572	0.1572	0.39	6.32	4.47	1.88	MIR_SB
2MASX J09063400+0451271	09:06:34.20	+04:51:25.0	0.1250	0.1230	0.1252	0.40	12.39	3.77	1.40	MIR_SB
SDSS J091127.61+055054.0	09:11:27.61	+05:50:54.1	2.7930	2.7877	-0.0218	0.11	1.57	3.46	0.30	MIR_AGN
2MASSi J0913454+405628	09:13:45.49	+40:56:28.2	0.4410	0.4361	0.4361	0.23	2.21	4.44	1.41	MIR_AGN2
2MASX J09141380+0322009	09:14:13.80	+03:22:01.0	0.1460	0.1456	0.1456	0.45	6.11	4.63	2.20	MIR_SB
Hydra A	09:18:05.70	-12:05:44.0	0.0540	0.0555	0.0555	0.23	2.23	3.75	0.59	MIR_AGN2
MRK 0704	09:18:26.00	+16:18:19.0	0.0290	0.5619	0.5619	0.22	1.16	3.90	0.93	MIR_AGNx
SDSS J092014.11+453157.2	09:20:14.11	+45:31:57.3	0.4030	0.4049	0.4049	0.13	1.70	3.43	-0.00	MIR_AGNx
UGC 05101	09:35:51.60	+61:21:11.0	0.0390	0.0387	0.0387	0.67	9.22	4.53	2.47	MIR_SB
NGC 2992	09:45:42.00	-14:19:35.0	0.0080	0.0080	0.0080	0.50	5.32	4.06	1.27	MIR_SB
PG 0946+301	09:49:41.10	+29:55:19.0	1.2160	1.2208	1.2208	0.09	1.19	4.13	0.45	MIR_AGN2
Mrk 1239	09:52:19.10	-01:36:43.4	0.0290	0.0263	0.0243	0.37	3.61	4.11	0.64	MIR_AGN1
2MASX J09530021+8127282	09:53:00.50	+81:27:28.0	0.1560	0.1525	0.1525	0.53	13.70	3.62	0.75	MIR_SB
2MASSi J0955045+170556	09:55:04.50	+17:05:56.0	0.1390	0.1343	0.1230	0.14	1.12	4.03	0.56	MIR_AGN1
MESSIER 081	09:55:33.20	+69:03:55.0	0.0010	0.0020	0.0020	0.37	1.31	4.46	2.40	MIR_SB
IRAS 09539+0857	09:56:34.30	+08:43:06.0	0.1290	0.1320	0.1320	0.68	33.59	3.80	0.68	MIR_SB
PG 0953+414	09:56:52.40	+41:15:22.0	0.2340	0.2386	0.2386	0.16	1.84	4.39	1.05	MIR_AGN1
NGC 3081	09:59:29.50	-22:49:35.0	0.0080	0.0060	0.0060	0.13	1.12	4.70	2.35	MIR_AGN2
3C 234	10:01:49.50	+28:47:09.0	0.1850	0.1853	0.1829	0.33	1.84	4.47	1.63	MIR_AGN1
NGC 3079	10:01:57.80	+55:40:47.0	0.0040	0.0060	0.0080	0.68	—	4.56	3.05	MIR_SB
PG 1001+054	10:04:20.10	+05:13:00.0	0.1605	0.1641	0.1641	0.12	1.28	4.08	0.58	MIR_AGN2
2MASSi J1005174+434609	10:05:17.43	+43:46:09.3	2.0970	1.9618	2.1956	0.13	1.05	3.89	0.74	MIR_AGN
2MASX J10062631+2725464	10:06:26.30	+27:25:46.0	0.1650	0.1595	0.1595	0.37	8.11	3.68	1.37	MIR_SB
PG 1004+130	10:07:26.10	+12:48:56.0	0.2410	0.1434	0.1434	0.15	1.84	4.10	1.31	MIR_AGN1
IRAS 10091+4704	10:12:16.70	+46:49:43.0	0.2460	0.2460	0.2460	0.48	6.50	4.34	1.47	MIR_SB
IRAS F10190+1322	10:21:42.50	+13:06:54.0	0.0770	0.0768	0.0746	0.48	8.19	4.35	2.24	MIR_SB
NGC 3227	10:23:30.60	+19:51:54.0	0.0040	0.0040	0.0040	0.70	14.48	4.43	1.51	MIR_SB
2MASSi J1027249+121920	10:27:25.00	+12:19:20.0	0.2310	0.2312	0.4917	0.17	2.08	4.55	1.25	MIR_AGN2
NGC 3256	10:27:51.27	-43:54:13.8	0.0084	0.0100	0.0100	0.85	66.77	5.20	3.21	MIR_SB
NGC 3281	10:31:52.10	-34:51:13.0	0.0110	0.0121	0.0790	0.28	1.45	5.40	3.54	MIR_AGN2
NGC 3310	10:38:45.96	+53:30:12.0	0.0047	0.0040	0.0060	0.41	2.34	4.48	2.26	MIR_SB
SDSS J103951.48+643004.2	10:39:51.49	+64:30:04.2	0.4020	1.0831	1.0831	0.10	1.17	4.16	0.74	MIR_AGN2
2MASX J10402919+1053178	10:40:29.20	+10:53:18.0	0.1360	0.1388	0.1388	0.64	10.92	4.08	1.15	unknown
SWIRE J104351.87+584953.7	10:43:51.87	+58:49:53.7	0.6090	0.6095	0.6159	0.06	1.02	2.60	-0.35	MIR_COMP
SDSS J104354.85+585901.3	10:43:54.82	+58:59:02.4	0.3500	1.0790	1.0055	0.07	1.15	3.07	-0.32	unknown
SWIRE J104406.30+583954.1	10:44:06.30	+58:39:54.1	2.4300	3.8730	3.8730	0.07	1.06	2.57	-0.75	MIR_AGN
SDSS J104407.97+584437.0	10:44:07.97	+58:44:37.0	0.5550	0.5526	0.5839	0.08	1.12	3.81	0.42	MIR_AGN2
SWIRE J104409.95+585224.8	10:44:09.95	+58:52:24.8	2.5400	0.4247	2.3527	0.07	1.13	3.14	-0.11	MIR_AGN
SWIRE J104613.4+585941	10:46:13.48	+58:59:41.4	3.6200	1.8858	3.3048	0.11	1.16	3.00	0.33	MIR_AGN

Table 1 (cont'd)

source ID (1)	RA (J2000.0) (2)	Dec (J2000.0) (3)	$z_{\rm spec}$ (4)	$z_{\rm MCPL}$ (5)	$z_{\rm ML}$ (6)	γ (7)	R (8)	$\log \mathcal{N}$ (9)	$\log \chi^2_{\rm ML}$ (10)	MIRclass (11)
NGC 3393	10:48:23.40	-25:09:43.0	0.0130	0.0121	0.3073	0.39	2.43	5.18	3.47	MIR_AGN2
IRAS 10485-1447	10:51:03.10	-15:03:22.0	0.1330	0.1297	0.1297	0.37	1.15	4.82	2.10	MIR_SB
2MASX J10514428+3539304	10:51:44.20	+35:39:31.0	0.1580	0.1572	0.1572	0.27	3.08	4.22	0.98	MIR_AGN2
ISO_LHDS J105148+573248	10:51:48.80	+57:32:48.0	0.9900	0.9855	0.9855	0.06	1.10	3.04	-0.84	MIR_AGN
2MASX J10522356+4408474	10:52:23.50	+44:08:48.0	0.0920	0.0920	0.0920	0.78	13.89	4.94	2.15	MIR_SB
SMM J105238.19+571651.1	10:52:38.19	+57:16:51.1	1.8520	1.8628	1.8400	0.19	1.36	2.19	-1.21	unknown
RDS 014Z	10:52:42.40	+57:31:58.4	1.3800	1.3534	1.3534	0.08	1.50	2.62	-0.32	MIR_AGN2
2MASX J10525269+5728597	10:52:52.80	+57:29:00.0	0.2050	0.2044	0.2068	0.22	2.75	3.22	-0.19	MIR_SB
[FFH2002] 113	10:53:05.60	+57:28:11.3	0.7920	3.6820	3.6913	0.12	1.82	2.65	-0.77	MIR_AGN
SDSS J105421.20+572544.2	10:54:21.30	+57:25:44.3	0.2050	0.2044	0.3743	0.09	1.38	3.42	-0.43	MIR_AGN1
SDSS J110213.99+380234.6	11:02:14.00	+38:02:35.0	0.1580	0.1572	0.1572	0.43	9.91	4.63	2.28	MIR_SB
NGC 3511	11:03:23.80	-23:05:12.0	0.0040	0.0040	0.0040	0.44	3.86	3.58	1.15	MIR_SB
PG 1100+772	11:04:13.70	+76:58:58.0	0.3110	0.3099	0.3099	0.15	1.81	4.43	0.94	MIR_AGN1
SDSS J110537.53+311432.2	11:05:37.50	+31:14:32.0	0.1990	0.1972	0.1972	0.37	4.60	4.28	1.27	MIR_SB
SDSS J110621.96+035747.1	11:06:21.96	+03:57:47.1	0.2420	0.2435	0.2435	0.17	2.36	3.23	0.00	MIR_AGN2
2MASSi J1106334-182123	11:06:33.40	-18:21:23.0	2.3050	2.3194	2.3194	0.06	1.02	3.80	0.64	MIR_AGN
NGC 3516	11:06:47.50	+72:34:07.0	0.0090	0.0080	0.0100	0.26	2.88	3.97	0.78	MIR_AGN2
MESSIER 108	11:11:30.97	+55:40:26.8	0.0032	0.0020	0.4680	0.38	1.18	5.07	3.07	MIR_SB
LCRS B110930.3-023804	11:12:03.40	-02:54:22.0	0.1060	0.1074	0.1074	0.79	19.36	4.26	1.82	MIR_SB
B2 1111+32	11:14:38.90	+32:41:33.0	0.1890	0.1876	0.6224	0.14	1.08	5.16	3.05	MIR_AGN2
AM 1113-270	11:15:31.60	-27:16:23.0	0.1360	0.1365	0.1365	0.72	9.70	3.97	1.19	MIR_SB
NGC 3628	11:20:17.02	+13:35:22.2	0.0023	0.0020	0.0020	0.87	—	4.57	2.65	MIR_SB
IRAS 11180+1623	11:20:41.70	+16:06:57.0	0.1660	0.1618	0.1618	0.64	12.36	3.81	1.01	MIR_SB
CGCG 011-076	11:21:12.20	-02:59:03.0	0.0250	0.0243	0.0243	0.47	8.47	3.90	0.96	MIR_SB
NGC 3660	11:23:32.20	-08:39:30.0	0.0120	0.0121	0.0121	0.24	1.77	3.39	0.33	MIR_SB
MRK 1298	11:29:16.60	-04:24:08.0	0.0620	0.3688	0.3688	0.11	1.01	4.31	1.76	MIR_AGN2
NGC 3783	11:39:01.70	-37:44:19.0	0.0097	0.0100	0.0100	0.13	1.02	4.54	2.00	MIR_AGN2
NGC 3786	11:39:42.50	+31:54:33.0	0.0090	0.0080	0.0100	0.26	3.71	4.93	2.65	MIR_SB
2MASXi J1141220+405950	11:41:22.00	+40:59:51.0	0.1490	0.1456	0.1502	0.35	4.16	4.55	2.10	MIR_SB
NGC 3862	11:45:05.00	+19:36:22.7	0.0217	0.0222	0.0222	0.25	3.83	4.26	1.04	MIR_AGN2
NGC 3894	11:48:50.30	+59:24:56.0	0.0108	0.0100	0.0121	0.19	2.72	4.32	1.52	MIR_AGN2
2MASX J11531422+1314276	11:53:14.20	+13:14:28.0	0.1270	0.1252	0.1252	0.54	15.34	4.89	2.28	MIR_SB
NGC 3982	11:56:28.10	+55:07:31.0	0.0040	0.0040	0.0040	0.43	3.95	3.76	1.01	MIR_SB
SDSS J115718.34+600345.6	11:57:18.35	+60:03:45.6	0.4906	0.4917	0.4917	0.18	2.18	3.87	0.47	MIR_AGN1
NGC 3998	11:57:56.10	+55:27:13.0	0.0035	0.0020	0.0020	0.16	1.71	4.21	1.86	MIR_AGN1
NGC 4051	12:03:09.60	+44:31:53.0	0.0020	0.0020	0.0020	0.36	2.24	4.08	0.72	MIR_AGN1
UGC 07064	12:04:43.30	+31:10:38.0	0.0250	0.0243	0.0263	0.36	3.22	3.67	0.54	MIR_SB
NGC 4088	12:05:34.19	+50:32:20.5	0.0031	0.0040	0.0040	0.46	5.68	4.25	1.62	MIR_SB
2MASX J12054771+1651085	12:05:47.70	+16:51:08.0	0.2170	0.2140	0.2140	0.40	11.03	3.98	1.50	MIR_SB
NGC 4151	12:10:32.60	+39:24:21.0	0.0030	0.0020	0.0020	0.75	9.06	5.88	4.05	MIR_AGN1
IRAS 12112+0305	12:13:46.00	+02:48:38.0	0.0730	0.0703	0.0703	0.84	8.46	4.24	1.50	MIR_SB
NGC 4194	12:14:09.64	+54:31:34.6	0.0095	0.0100	0.0100	0.81	—	4.70	2.37	MIR_SB
PG 1211+143	12:14:17.70	+14:03:13.0	0.0810	0.0790	0.0790	0.21	1.30	5.01	2.07	MIR_AGN1
IRAS 12127-1412	12:15:18.90	-14:29:45.0	0.1330	0.1365	0.1320	0.17	2.59	4.38	2.84	MIR_AGN2
NGC 4253	12:18:26.50	+29:48:46.0	0.0130	0.0121	0.0121	0.54	6.88	4.06	0.71	MIR_AGN2
NGC 4261	12:19:23.20	+5:49:30.8	0.0074	0.0080	0.0060	0.18	1.46	4.56	1.83	MIR_AGN2
NGC 4385	12:25:42.67	+00:34:20.4	0.0071	0.0060	0.0060	0.34	1.71	4.34	1.93	MIR_SB
NGC 4388	12:25:46.70	+12:39:44.0	0.0080	0.0080	0.0080	0.60	6.72	4.17	1.52	MIR_SB
3C 273	12:29:06.70	+02:03:09.0	0.1583	0.1641	0.1641	0.27	1.87	5.09	2.21	MIR_AGN2
MESSIER 088	12:31:59.20	+14:25:14.0	0.0080	0.0080	0.0080	0.22	1.62	3.45	0.80	MIR_SB
MRK 0771	12:32:03.60	+20:09:29.0	0.0630	0.0640	0.0640	0.14	1.58	4.81	1.38	MIR_AGN1
LBQS 1230+1627B	12:33:10.40	+16:10:52.0	2.7350	2.7350	2.7350	0.07	1.02	3.74	0.35	MIR_AGN
NGC 4507	12:35:36.60	-39:54:33.0	0.0120	0.0121	0.0121	0.43	3.13	5.52	3.70	MIR_AGN2
SMM J123555.1+620901	12:35:55.13	+62:09:01.6	1.8750	1.8685	1.8343	0.16	2.65	2.33	-0.35	MIR_COMP
GOODS J123600.15+621047.5	12:36:00.16	+62:10:47.3	2.0020	0.4593	2.0156	0.06	1.22	3.02	-0.18	MIR_COMP
SDSS J123603.25+621111.1	12:36:03.25	+62:11:10.8	0.6380	0.6420	0.6420	0.32	11.77	2.92	-0.21	MIR_SB
GN 850.07	12:36:21.27	+62:17:08.1	1.9920	2.0156	1.9677	0.11	1.01	2.33	-0.41	unknown

Table 1 (cont'd)

source ID (1)	RA (J2000.0) (2)	Dec (J2000.0) (3)	$z_{\rm spec}$ (4)	$z_{\rm MCPL}$ (5)	$z_{\rm ML}$ (6)	γ (7)	R (8)	$\log \mathcal{N}$ (9)	$\log \chi^2_{\rm ML}$ (10)	MIRclass (11)
SDSS J123622.50+621544.4	12:36:22.48	+62:15:44.3	0.6390	0.6354	1.8858	0.17	2.79	2.77	0.33	MIR_SB
SDSS J123633.25+620834.6	12:36:33.22	+62:08:34.7	0.9340	0.9346	0.9346	0.18	3.86	2.64	-0.41	unknown
FFN 228	12:36:34.51	+62:12:40.9	1.2190	1.2163	1.2252	0.24	3.83	2.80	-0.24	MIR_SB
GOODS J123655.94+620808.6	12:36:55.93	+62:08:08.1	0.7920	0.7930	0.7894	0.24	4.87	2.68	-0.31	MIR_COMP
GOODS J123704.33+621446.6	12:37:04.34	+62:14:46.1	2.2110	0.2262	0.6095	0.10	1.31	2.41	-0.62	unknown
[BI2006] J123707.176+621408.	12:37:07.19	+62:14:08.0	2.4900	2.4687	2.5035	0.24	5.32	2.00	-0.93	unknown
SMM J123711.1+621325	12:37:11.37	+62:13:31.1	1.9960	1.9856	1.9856	0.24	3.75	2.30	-0.55	MIR_SB
SMM J123711.9+621331	12:37:11.97	+62:13:25.8	1.9920	1.9856	2.0036	0.22	3.61	2.09	-0.70	MIR_SB
SDSS J123716.59+621643.9	12:37:16.59	+62:16:43.2	0.5570	1.8061	1.7949	0.25	2.88	2.57	-0.38	MIR_SB
GOODS J123726.51+622026.8	12:37:26.49	+62:20:26.6	1.8600	1.7232	1.7232	0.13	2.06	2.43	-0.57	MIR_AGN2
SDSS J123734.60+621723.2	12:37:34.52	+62:17:23.2	0.6410	0.6387	0.6354	0.27	6.55	2.96	0.01	MIR_SB
MESSIER 058	12:37:43.50	+11:49:05.0	0.0050	0.5218	0.0060	0.20	1.44	4.14	1.81	MIR_SB
NGC 4593	12:39:39.40	-05:20:39.0	0.0090	0.0080	0.0100	0.26	2.67	4.79	2.07	MIR_AGN1
MESSIER 104	12:39:59.40	-11:37:23.0	0.0030	0.0040	0.0040	0.47	3.04	4.14	1.79	MIR_SB
NGC 4602	12:40:36.50	-05:07:55.0	0.0080	0.0080	0.0080	0.39	2.11	3.47	0.38	MIR_SB
IC 3639	12:40:52.80	-36:45:21.0	0.0110	0.0141	0.0141	0.36	2.92	4.19	1.11	MIR_AGN2
NGC 4676	12:46:10.10	+30:43:55.0	0.0225	0.0243	0.0243	0.39	4.39	4.38	2.23	MIR_SB
PG 1244+026	12:46:35.20	+02:22:09.0	0.0480	0.0471	0.1118	0.13	2.20	4.19	0.78	MIR_AGN1
FBQS J124707.7+370536	12:47:07.70	+37:05:37.0	0.1580	0.1595	0.1595	0.37	2.40	4.60	1.72	MIR_SB
NGC 4748	12:52:12.40	-13:24:53.0	0.0150	0.0141	0.0141	0.38	4.78	3.64	0.76	MIR_SB
UGC 08058	12:56:14.20	+56:52:25.0	0.0420	0.0408	0.0450	0.40	3.28	5.97	4.40	MIR_AGN2
NGC 4818	12:56:48.90	-08:31:31.1	0.0022	0.0020	-0.0020	0.58	6.35	4.70	2.50	MIR_SB
FBQS J125807.4+232921	12:58:07.40	+23:29:22.0	0.2590	0.2661	0.2661	0.22	3.02	4.57	1.10	MIR_AGN2
2MASX J13000533+1632151	13:00:05.30	+16:32:15.0	0.0800	0.0920	0.0920	0.22	1.30	4.78	1.81	MIR_AGNx
NGC 4922	13:01:24.90	+29:18:40.0	0.0240	0.0243	0.0243	0.43	6.49	4.20	2.15	MIR_AGN2
NGC 4941	13:04:13.10	-05:33:06.0	0.0040	0.0040	0.0040	0.31	3.55	4.16	1.26	MIR_AGN2
NGC 4939	13:04:14.40	-10:20:23.0	0.0104	0.0100	0.0100	0.38	3.39	4.82	2.49	MIR_AGN2
NGC 4945	13:05:27.48	-49:28:05.6	0.0009	0.0040	0.0040	0.66	—	5.20	4.70	MIR_SB
PG 1302-102	13:05:33.00	-10:33:19.0	0.2780	0.2788	0.2788	0.10	1.92	4.83	1.35	MIR_AGN1
NGC 4968	13:07:06.00	-23:40:37.0	0.0098	0.0100	0.0100	0.54	4.16	3.99	0.84	MIR_AGN2
PG 1307+085	13:09:47.00	+08:19:48.0	0.1550	0.1549	0.1525	0.10	1.86	4.82	1.44	MIR_AGN1
NGC 5005	13:10:56.20	+37:03:33.0	0.0030	0.0020	0.0020	0.37	2.50	3.90	1.69	MIR_SB
FBQS J131217.7+351521	13:12:17.80	+35:15:21.0	0.1840	0.1805	0.1805	0.28	4.42	4.56	1.20	MIR_AGN1
IRAS 13106-0922	13:13:14.80	-09:38:00.0	0.1745	0.1711	0.1711	0.26	3.78	3.89	2.15	MIR_SB
NGC 5033	13:13:27.50	+36:35:38.0	0.0030	0.0040	0.0040	0.59	3.42	4.45	2.67	MIR_SB
MCG -03-34-063	13:22:19.00	-16:42:30.0	0.0210	0.0202	0.0202	0.32	5.13	3.19	0.14	MIR_SB
SDSS J132323.33-015941.9	13:23:23.33	-01:59:41.9	0.3503	0.3498	0.3498	0.18	2.96	3.57	0.35	MIR_AGN2
[HB89] 1321+058	13:24:19.90	+05:37:05.0	0.2051	0.2044	0.2386	0.20	1.07	4.52	2.62	MIR_AGN2
NGC 5128	13:25:27.60	-43:01:09.0	0.0020	0.0020	0.0020	0.76	—	4.78	2.60	MIR_AGN2
NGC 5135	13:25:44.00	-29:50:01.0	0.0140	0.0141	0.0141	0.69	9.36	4.16	1.40	MIR_SB
MESSIER 051a	13:29:52.70	+47:11:43.0	0.0020	0.0020	0.0020	0.75	7.99	4.58	2.75	MIR_SB
ESO 383- G 035	13:35:53.80	-34:17:44.0	0.0080	0.0060	0.0060	0.38	3.34	5.29	2.75	MIR_AGN1
IRAS 13335-2612	13:36:22.30	-26:27:34.0	0.1250	0.1230	0.1230	0.42	11.59	3.96	1.40	MIR_SB
2MASX J13362406+3917305	13:36:24.10	+39:17:31.0	0.1793	0.1782	0.1782	0.38	2.86	4.24	1.21	MIR_AGN1
IC 4296	13:36:39.00	-33:57:57.2	0.0124	0.0121	0.0121	0.20	1.43	4.26	1.55	MIR_AGN2
[HB89] 1334+246	13:37:18.70	+24:23:03.0	0.1080	0.1096	0.1096	0.51	3.62	5.47	2.66	MIR_AGN1
NGC 5256	13:38:17.50	+48:16:37.0	0.0280	0.0284	0.0284	0.58	10.07	3.89	1.20	MIR_SB
MRK 0273	13:44:42.10	+55:53:13.0	0.0380	0.0387	0.0387	0.55	1.10	4.55	2.28	MIR_SB
4C +12.50	13:47:33.30	+12:17:24.0	0.1217	0.1207	0.1207	0.32	3.07	5.15	2.22	MIR_AGN2
2MASX J13484011+5818522	13:48:40.20	+58:18:52.0	0.1580	0.1525	0.1525	0.65	7.68	4.73	1.66	MIR_SB
IC 4329A	13:49:19.20	-30:18:34.0	0.0160	0.0161	0.0854	0.34	1.21	4.24	1.41	MIR_AGN2
UGC 08782	13:52:17.80	+31:26:46.5	0.0450	0.0450	0.0471	0.35	5.89	4.51	2.06	MIR_SB
PG 1351+640	13:53:15.80	+63:45:46.0	0.0880	0.0876	0.0876	0.29	3.44	4.37	1.65	MIR_AGN1
NGC 5347	13:53:17.80	+33:29:27.0	0.0080	0.0080	0.1572	0.34	1.38	5.34	2.89	MIR_AGN2
SDSS J135331.57+042805.2	13:53:31.60	+04:28:05.0	0.1360	0.1365	0.1343	0.41	8.04	3.95	1.50	MIR_SB
MRK 0463	13:56:02.90	+18:22:19.0	0.0503	0.0492	0.0471	0.40	3.17	5.54	3.27	MIR_AGN2
2MASX J13561001+2905355	13:56:10.00	+29:05:35.0	0.1080	0.1074	0.1074	0.47	1.25	4.85	2.16	MIR_SB

Table 1 (cont'd)

source ID (1)	RA (J2000.0) (2)	Dec (J2000.0) (3)	$z_{\rm spec}$ (4)	$z_{\rm MCPL}$ (5)	$z_{\rm ML}$ (6)	γ (7)	R (8)	$\log \mathcal{N}$ (9)	$\log \chi^2_{\rm ML}$ (10)	MIRclass (11)
2MASX J14025121+2631175	14:02:51.20	+26:31:18.0	0.1870	0.1185	0.1185	0.09	1.08	3.43	-0.69	MIR_AGN1
[HB89] 1402+436	14:04:38.80	+43:27:07.0	0.3233	0.3444	0.3444	0.19	1.72	4.23	0.94	MIR_AGN1
FBQS J1405+2555	14:05:16.20	+25:55:34.0	0.1640	0.1618	0.2737	0.18	1.27	4.75	1.71	MIR_AGN1
MRK 0668	14:07:00.40	+28:27:15.0	0.0766	0.0790	0.0790	0.27	2.58	4.60	2.00	MIR_AGN1
2MASX J14081899+2904474	14:08:19.00	+29:04:47.0	0.1170	0.1185	0.1185	0.45	8.14	4.93	2.60	MIR_SB
SBS 1408+567	14:09:55.57	+56:28:26.5	2.5830	2.7500	1.6854	0.08	1.21	4.33	0.94	MIR_AGN
3C 295	14:11:20.60	+52:12:09.0	0.4610	2.8411	0.3634	0.07	1.03	3.61	0.30	MIR_AGN2
NGC 5506	14:13:14.90	-03:12:27.0	0.0060	0.0060	0.0060	0.55	4.24	4.30	1.83	MIR_AGN2
PG 1411+442	14:13:48.30	+44:00:14.0	0.0896	0.0898	0.1411	0.09	1.23	5.01	1.43	MIR_AGN1
IRAS F14121-0126	14:14:45.50	-01:40:55.0	0.1502	0.1502	0.1502	0.44	7.71	4.63	2.20	MIR_SB
[HB89] 1413+117	14:15:46.27	+11:29:43.4	2.5580	2.5529	2.5529	0.16	1.47	4.59	1.04	MIR_AGN
[HB89] 1413+135	14:15:58.80	+13:20:24.0	0.2467	0.2460	0.2560	0.12	1.31	4.06	1.28	MIR_AGN2
NGC 5548	14:17:59.50	+25:08:12.0	0.0170	0.0182	0.1456	0.36	1.88	5.22	2.82	MIR_AGN1
3C 298	14:19:08.20	+06:28:35.0	1.4360	1.4396	1.6322	0.09	1.22	4.03	0.38	MIR_AGN2
SDSS J142211.65+075927.9	14:22:11.60	+07:59:28.0	0.1310	0.1320	0.1320	0.34	3.35	4.56	1.43	MIR_SB
IRAS F14202+2615	14:22:31.40	+26:02:05.0	0.1587	0.1595	0.1595	0.45	8.44	4.80	2.36	MIR_SB
UGC 09214	14:22:55.40	+32:51:03.0	0.0340	0.0346	0.0346	0.28	3.49	3.89	1.50	MIR_SB
SDSS J142614.83+350616.0	14:26:14.87	+35:06:16.5	0.2168	0.2165	0.3073	0.09	1.20	3.97	0.27	MIR_AGN2
FLX J142644.33+333051.7	14:26:44.34	+33:30:52.0	3.3550	1.5391	3.4093	0.23	2.47	3.23	0.17	MIR_AGN
2MASX J14280106-1603400	14:28:01.10	-16:03:39.0	0.1490	0.1479	0.1479	0.41	5.98	4.56	1.83	MIR_SB
SST24 J142827.1+354127	14:28:27.19	+35:41:27.7	1.2930	1.2702	1.2702	0.22	3.75	4.02	1.15	MIR_AGN2
SDSS J142843.02+342411.8	14:28:42.96	+34:24:09.9	2.1800	3.0949	0.6954	0.09	1.43	3.44	0.01	MIR_AGN
MRK 1383	14:29:06.60	+01:17:06.0	0.0870	0.0854	0.1900	0.22	1.39	4.49	1.18	MIR_AGN1
IRAC J142939.1+353557	14:29:39.18	+35:35:58.4	2.4980	2.4479	2.5886	0.07	1.07	2.63	-0.72	unknown
SDSS J143132.13+341417.3	14:31:32.17	+34:14:17.9	1.0370	1.0337	1.0337	0.14	1.79	3.18	-1.21	MIR_AGN1
SDSS J143156.37+325137.6	14:31:56.40	+32:51:38.1	0.4120	0.4190	0.4077	0.09	1.01	3.96	0.32	MIR_AGN1
FBQS J1431+3416	14:31:57.96	+34:16:50.1	0.7155	0.7193	0.7193	0.15	2.60	4.20	0.71	MIR_AGN1
NGC 5643	14:32:40.80	-44:10:29.0	0.0040	0.0040	0.0040	0.62	4.03	5.55	3.28	MIR_AGN2
SDSS J143310.30+334604.3	14:33:10.33	+33:46:04.5	2.4000	2.4136	2.4136	0.09	1.10	4.04	0.22	MIR_AGN
NGC 5674	14:33:52.20	+05:27:30.0	0.0250	0.0243	0.0243	0.25	3.98	4.09	1.33	MIR_SB
SST24 J143424.4+334543	14:34:24.50	+33:45:43.3	2.2630	2.3729	2.3527	0.09	1.05	2.97	-0.21	unknown
UGC 09412	14:36:22.10	+58:47:39.0	0.0310	0.0325	0.0325	0.28	2.19	3.98	0.60	MIR_AGN1
SDSS J143728.77+344547.2	14:37:28.80	+34:45:47.6	0.6200	0.6420	0.6420	0.12	1.60	4.29	0.92	MIR_AGN2
2MASX J14373831-1500239	14:37:38.30	-15:00:23.0	0.0830	0.0833	0.0833	0.42	1.21	5.12	2.76	MIR_SB
[HB89] 1435-067	14:38:16.10	-06:58:21.0	0.1260	0.0768	0.0768	0.14	2.40	4.11	0.44	MIR_AGN1
3C 303.1	14:43:14.80	+77:07:29.0	0.2670	0.2686	0.2661	0.20	1.96	3.87	0.77	MIR_AGN2
PG 1448+273	14:51:08.70	+27:09:27.0	0.0650	0.0661	0.0661	0.12	1.79	4.23	0.86	MIR_AGN1
IRAS 14484-2434	14:51:23.80	-24:46:30.0	0.1480	0.1456	0.1456	0.47	10.83	4.11	1.66	MIR_SB
2MASX J15011320+2329085	15:01:13.20	+23:29:08.0	0.2580	0.2535	0.2535	0.16	1.91	3.82	-0.06	MIR_AGN2
SDSS J150539.56+574307.2	15:05:39.50	+57:43:07.0	0.1505	0.1456	0.1456	0.48	10.89	4.15	1.96	MIR_SB
2MASX J15115979-2119015	15:11:59.80	-21:19:02.0	0.0446	0.0471	0.0471	0.08	2.02	4.45	0.71	MIR_AGN
UGC 09799	15:16:44.40	+07:01:16.6	0.0344	0.0346	2.1074	0.08	1.47	3.42	0.33	MIR_AGN2
2MASSi J1516532+190048	15:16:53.20	+19:00:48.0	0.1900	0.2386	0.2386	0.33	2.90	3.86	0.05	MIR_AGN1
SDSS J152238.10+333135.8	15:22:38.00	+33:31:36.0	0.1250	0.1230	0.1230	0.46	4.03	4.27	1.77	MIR_SB
2MASX J15244389+2340099	15:24:43.90	+23:40:10.0	0.1390	0.1388	0.1388	0.47	9.93	4.16	1.62	MIR_SB
NGC 5929	15:26:06.10	+41:40:14.0	0.0080	0.0080	0.0060	0.25	2.24	3.35	0.22	MIR_SB
3C 321	15:31:43.40	+24:04:19.0	0.0960	0.0963	0.0963	0.31	2.81	4.98	2.74	MIR_AGN2
NGC 5953	15:34:32.40	+15:11:38.0	0.0070	0.0060	0.0080	0.51	3.24	5.21	3.27	MIR_SB
ARP 220	15:34:57.10	+23:30:11.0	0.0180	0.0161	0.0161	0.51	1.36	5.93	4.15	MIR_SB
[HB89] 1543+489	15:45:30.20	+48:46:09.0	0.3996	0.8662	0.8662	0.17	1.10	4.84	1.53	MIR_AGN1
[HB89] 1545+210	15:47:43.50	+20:52:17.0	0.2640	0.2611	0.2611	0.15	1.74	4.04	0.64	MIR_AGN1
NGC 5995	15:48:24.90	-13:45:28.0	0.0250	0.0263	0.0243	0.31	3.19	4.01	0.90	MIR_SB
IRAS 15462-0450	15:48:56.80	-04:59:34.0	0.0998	0.1007	0.1007	0.47	2.18	5.21	2.83	MIR_AGN2
2MASX J15504152-0353175	15:50:41.50	-03:53:18.0	0.0303	0.0304	0.1185	0.41	1.95	3.85	0.75	MIR_AGN1
SDSS J160250.95+545057.8	16:02:50.96	+54:50:58.1	1.1970	0.3073	1.2252	0.07	1.13	3.09	-0.55	MIR_AGN1
SDSS J160418.97+541524.3	16:04:19.01	+54:15:24.4	1.4770	2.0888	2.2537	0.09	1.26	3.34	-0.56	MIR_AGN2
SDSS J160437.80+534957.6	16:04:37.83	+53:49:57.8	0.9560	0.9618	2.5035	0.08	1.01	2.83	-0.68	MIR_AGN

Table 1 (cont'd)

source ID (1)	RA (J2000.0) (2)	Dec (J2000.0) (3)	$z_{\rm spec}$ (4)	$z_{\rm MCPL}$ (5)	$z_{\rm ML}$ (6)	γ (7)	R (8)	$\log \mathcal{N}$ (9)	$\log \chi^2_{\rm ML}$ (10)	MIRclass (11)
SDSS J160637.87+535008.4	16:06:37.87	+53:50:08.6	2.9430	1.1943	1.6165	0.08	1.06	3.48	0.05	MIR_AGN
SDSS J161007.11+535814.0	16:10:07.11	+53:58:14.0	2.0150	1.8800	1.8800	0.09	1.28	3.61	0.06	MIR_AGN1
2MASX J16114042-0147062	16:11:40.50	-01:47:06.0	0.1340	0.1343	0.1343	0.57	14.45	5.04	2.51	MIR_SB
2MASSi J1612399+471157	16:12:39.90	+47:11:57.0	2.3961	2.3729	2.3729	0.10	1.48	3.60	0.13	MIR_AGN
SDSS J161259.28+541503.5	16:12:59.27	+54:15:03.9	1.1700	1.1724	1.1724	0.16	3.65	2.95	-0.59	MIR_COMP
MRK 0876	16:13:57.20	+65:43:10.0	0.1290	0.1297	0.1297	0.22	2.64	4.93	2.15	MIR_AGN1
SDSS J161401.08+544733.1	16:14:01.09	+54:47:33.2	0.3870	0.3993	1.6746	0.11	1.61	3.27	-0.43	MIR_AGNx
SDSS J161526.63+543005.9	16:15:26.63	+54:30:06.3	1.3670	1.1681	1.4009	0.07	1.23	2.87	-0.62	MIR_AGN1
SDSS J161543.52+544828.7	16:15:43.52	+54:48:28.8	1.6920	1.5749	1.5647	0.10	1.38	3.53	0.22	MIR_AGN1
SDSS J161551.30+550723.0	16:15:51.31	+55:07:23.3	1.1000	1.0956	1.0956	0.13	2.23	3.06	-0.52	MIR_AGN2
MRK 0877	16:20:11.30	+17:24:28.0	0.1120	0.1163	0.1343	0.06	1.15	4.78	1.03	MIR_AGN1
SBS 1626+554	16:27:56.10	+55:22:32.0	0.1330	0.1320	0.1549	0.09	1.74	4.44	1.00	MIR_AGN1
VV 807	16:29:52.90	+24:26:38.0	0.0380	0.0387	0.0387	0.40	6.08	4.08	1.51	MIR_SB
SDSS J163221.37+155145.5	16:32:21.40	+15:51:46.0	0.2420	0.2411	0.2411	0.73	29.54	4.64	1.59	MIR_SB
NGC 6251	16:32:31.90	+82:32:16.4	0.0247	0.0263	0.0161	0.22	2.08	4.23	1.58	MIR_AGN1
SDSS J163425.11+404152.4	16:34:25.13	+40:41:52.6	1.6920	1.3022	2.0156	0.06	1.02	3.17	-0.51	MIR_AGN1
SDSS J163428.13+412742.6	16:34:28.15	+41:27:42.6	0.4050	0.4049	1.0583	0.19	1.25	2.92	-0.44	MIR_SB
IRAS 16334+4630	16:34:52.60	+46:24:53.0	0.1910	0.1900	0.1853	0.49	10.05	3.90	1.36	MIR_SB
SDSS J163531.05+410027.3	16:35:31.09	+41:00:27.4	1.1520	1.1508	1.1252	0.11	1.38	3.61	0.17	MIR_AGN1
SDSS J163553.63+412056.0	16:35:53.65	+41:20:55.8	1.1950	1.2208	1.2208	0.16	1.59	3.12	-0.46	MIR_AGN2
MM J163639+4056	16:36:39.01	+40:56:35.9	1.4950	1.4839	1.4839	0.13	1.87	2.39	-0.81	MIR_COMP
MM J163655+4059	16:36:55.78	+40:59:10.1	2.5920	3.1031	2.6030	0.10	1.16	2.99	-0.55	MIR_AGN
SMM J163658.78+405728.1	16:36:58.78	+40:57:28.1	1.1920	1.2075	1.2075	0.12	1.80	2.17	-0.72	unknown
2MASSi J1637002+222114	16:37:00.20	+22:21:14.0	0.2110	0.2116	0.2116	0.25	2.23	4.20	1.00	MIR_AGN2
B3 1635+416	16:37:02.23	+41:30:22.2	1.1790	1.0055	1.1423	0.18	1.83	3.54	-0.02	MIR_AGN1
MM J163706+4053	16:37:06.60	+40:53:14.0	2.3745	2.3729	2.3662	0.14	1.02	2.35	-0.65	unknown
SDSS J163721.21+411502.7	16:37:21.23	+41:15:02.6	2.3560	3.1031	1.4939	0.17	1.25	2.90	-0.13	unknown
SDSS J163739.29+405643.6	16:37:39.30	+40:56:43.4	1.4380	1.4445	0.7400	0.14	1.31	3.15	-0.46	MIR_AGN2
SDSS J163739.43+414348.0	16:37:39.45	+41:43:48.0	1.4140	0.9346	0.9384	0.11	1.30	3.48	0.55	MIR_AGN1
SDSS J163847.42+421141.7	16:38:47.43	+42:11:41.8	1.7710	1.6961	1.9856	0.09	1.58	3.40	-0.07	MIR_AGN1
SDSS J163930.82+410013.6	16:39:30.83	+41:00:13.7	1.0520	0.9423	0.9191	0.10	1.32	2.99	-0.63	MIR_AGN1
SDSS J163952.85+410344.8	16:39:52.86	+41:03:44.8	1.6030	1.5240	1.5595	0.12	1.57	3.40	-0.10	MIR_AGN1
2MASSi J1640100+410522	16:40:10.14	+41:05:22.4	1.0990	1.0956	1.0956	0.09	1.15	3.68	-0.20	MIR_AGN1
SDSS J164016.08+412101.2	16:40:16.09	+41:21:01.4	1.7620	1.1638	2.0277	0.08	1.27	3.52	0.01	MIR_AGNx
SDSS J164018.34+405813.0	16:40:18.34	+40:58:13.1	1.3160	1.3068	1.3068	0.10	1.37	3.22	-0.59	MIR_AGN1
SDSS J1641+3858	16:41:31.73	+38:58:40.9	0.5960	0.5967	0.5967	0.21	3.62	3.29	-0.35	MIR_AGN2
IRAS 16468+5200	16:48:01.60	+51:55:45.0	0.1500	0.1525	0.1525	0.36	1.32	4.72	1.88	MIR_SB
2MASX J16491420+3425096	16:49:14.20	+34:25:10.0	0.1110	0.1118	0.1096	0.37	6.70	5.00	2.77	MIR_SB
2MASSi J1649149+530316	16:49:14.90	+53:03:16.0	2.2600	2.5317	2.5317	0.08	1.04	3.80	0.42	MIR_AGN
SBS 1648+547	16:49:47.00	+54:42:35.0	0.1040	0.0985	0.0985	0.50	1.10	5.00	2.47	MIR_SB
2MASSi J1659397+183436	16:59:39.80	+18:34:37.0	0.1707	0.1711	0.1711	0.33	3.75	4.78	1.47	MIR_AGN1
[HB89] 1700+518	17:01:24.80	+51:49:20.0	0.2920	0.2917	0.2917	0.34	6.06	4.82	0.02	MIR_AGN1
IRAS F17028+5817	17:03:41.90	+58:13:45.0	0.1060	0.1051	0.1051	0.75	12.53	4.85	1.92	MIR_SB
IRAS 17044+6720	17:04:28.40	+67:16:23.0	0.1350	0.1388	0.1388	0.45	9.68	5.15	2.63	MIR_AGN2
SBS 1704+608	17:04:41.40	+60:44:31.0	0.3710	0.3743	0.0746	0.24	2.98	4.71	1.75	MIR_AGN1
IRAS F17068+4027	17:08:31.90	+40:23:28.0	0.1790	0.1782	0.1782	0.56	13.65	4.10	1.58	MIR_SB
SDSS J171021.76+591854.7	17:10:21.76	+59:18:54.7	0.4186	0.4218	0.4218	0.18	2.39	4.13	0.59	MIR_AGN2
SDSS J171106.82+590436.7	17:11:06.80	+59:04:36.0	0.4620	0.4563	0.4563	0.26	5.10	3.01	-0.30	MIR_COMP
SDSS J171117.65+584123.8	17:11:17.66	+58:41:23.8	0.6170	0.6387	0.6063	0.11	1.15	3.73	0.39	MIR_AGN1
SDSS J171126.94+585544.1	17:11:26.94	+58:55:44.2	0.5370	0.5402	0.5402	0.12	1.77	3.04	-0.89	MIR_AGN1
SSTXFLS J171138.5+583836	17:11:38.59	+58:38:36.7	2.4690	2.4965	2.4965	0.19	1.27	2.41	-1.36	MIR_AGN2
SDSS J171147.48+585840.1	17:11:47.40	+58:58:39.0	0.7997	0.8002	0.8038	0.14	1.61	3.84	0.12	MIR_AGN2
SDSS J171207.44+584754.4	17:12:07.43	+58:47:54.4	0.2693	0.2485	3.7670	0.08	1.11	4.08	0.60	MIR_AGN1
FLS22(R) J171215.4+585227	17:12:15.44	+58:52:27.9	1.0510	1.0460	1.0014	0.08	1.27	3.44	0.17	MIR_AGN2
SDSS J171238.46+594233.6	17:12:38.50	+59:42:33.4	0.5610	0.5651	0.5651	0.12	1.48	3.10	0.21	MIR_SB
SDSS J171302.41+593611.1	17:13:02.37	+59:36:11.0	0.6680	0.6651	0.6651	0.15	2.55	3.08	0.13	MIR_AGN2
SDSS J171312.08+600840.4	17:13:12.00	+60:08:40.2	0.7594	0.7610	0.7610	0.39	7.68	2.94	-0.74	MIR_SB

Table 1 (cont'd)

source ID (1)	RA (J2000.0) (2)	Dec (J2000.0) (3)	$z_{\rm spec}$ (4)	$z_{\rm MCPL}$ (5)	$z_{\rm ML}$ (6)	γ (7)	R (8)	$\log \mathscr{N}$ (9)	$\log \chi^2_{\rm ML}$ (10)	MIRclass (11)
SDSS J171313.96+603146.5	17:13:13.96	+60:31:46.6	0.1050	0.1900	0.1900	0.09	1.16	4.05	0.22	MIR_AGN1
SDSS J171324.17+585549.1	17:13:24.10	+58:55:49.0	0.6090	0.6420	0.1320	0.10	1.27	3.72	0.50	MIR_AGN2
SDSS J171334.02+595028.3	17:13:34.03	+59:50:28.3	0.6150	0.6159	0.6095	0.14	2.08	3.80	0.62	MIR_AGN1
SDSS J171335.16+584756.0	17:13:35.15	+58:47:56.1	0.1340	0.1343	0.1343	0.19	3.27	4.33	0.41	MIR_AGN2
SDSS J171352.41+584201.2	17:13:52.41	+58:42:01.2	0.5209	0.5218	0.5279	0.20	2.70	4.28	0.82	MIR_AGN1
SDSS J171433.73+592119.3	17:14:33.68	+59:21:19.3	0.9060	0.9077	0.9077	0.06	1.05	2.58	-1.52	MIR_AGN2
SSTXFLS J171448.5+594641	17:14:48.54	+59:46:41.1	0.8340	0.8365	0.8365	0.33	5.29	3.26	0.10	MIR_SB
SSTXFLS J171456.2+583816	17:14:56.24	+58:38:16.2	1.6370	1.6428	1.6428	0.08	1.43	3.23	0.33	MIR_AGN2
SDSS J171458.23+592411.2	17:14:58.27	+59:24:11.2	0.9370	0.9384	0.9384	0.25	3.66	2.61	-1.17	MIR_SB
SDSS J171506.56+583939.8	17:15:06.60	+58:39:39.7	0.7910	0.7894	0.7894	0.11	2.28	3.48	0.29	MIR_SB
SDSS J171530.74+600216.3	17:15:30.75	+60:02:16.4	0.4204	0.4247	0.4247	0.20	3.58	3.00	-0.75	MIR_AGN2
SSTXFLS J171535.7+602825	17:15:35.78	+60:28:25.5	2.4430	2.4548	2.4548	0.17	3.72	2.52	-1.41	MIR_AGN2
SDSS J171708.66+591341.0	17:17:08.70	+59:13:41.1	0.6460	0.6453	3.8633	0.15	3.23	3.21	-0.69	MIR_AGN1
SDSS J171736.90+593011.4	17:17:36.91	+59:30:11.5	0.5990	0.6127	0.5341	0.06	1.02	3.70	0.53	MIR_AGNx
SDSS J171748.42+594820.6	17:17:48.43	+59:48:20.6	0.7630	0.7262	0.7158	0.13	2.40	3.62	0.35	MIR_AGN1
SDSS J171755.10+592845.3	17:17:55.10	+59:28:45.3	0.2393	0.2411	0.2336	0.29	4.23	2.89	-0.64	MIR_SB
SDSS J171818.14+584905.2	17:18:18.14	+58:49:05.2	0.6340	0.6387	0.6387	0.16	1.06	3.06	-0.65	MIR_AGN1
SDSS J171831.70+595317.4	17:18:31.70	+59:53:17.0	0.7000	0.7056	0.6988	0.16	1.10	3.12	-0.59	MIR_AGN2
XFLS CH1 J171834.9+594534	17:18:34.90	+59:45:34.1	0.7363	0.7365	0.7365	0.28	5.79	2.99	-0.61	MIR_SB
SDSS J171839.74+593359.6	17:18:39.73	+59:33:59.6	0.3825	0.3826	0.3826	0.12	2.00	3.50	-0.19	MIR_AGN1
SSTXFLS J171844.8+600115	17:18:44.77	+60:01:15.9	2.0080	1.9856	1.9856	0.26	4.80	2.87	0.15	unknown
SDSS J171852.71+591432.0	17:18:52.71	+59:14:32.0	0.3220	0.3257	0.3257	0.26	4.68	4.02	0.88	MIR_SB
SDSS J171902.28+593715.9	17:19:02.29	+59:37:15.9	0.1783	0.1118	0.1118	0.09	1.12	4.35	0.68	MIR_AGN1
SDSS J171951.46+584222.8	17:19:51.40	+58:42:22.8	0.7002	0.6988	0.7022	0.24	3.23	3.47	0.24	MIR_SB
SSTXFLS J172000.2+601520	17:20:00.32	+60:15:20.9	0.9870	0.9815	0.9855	0.19	1.92	3.11	0.20	MIR_SB
SSTXFLS J172059.7+591125	17:20:59.80	+59:11:25.7	0.8240	0.8256	0.8256	0.26	6.11	3.00	0.13	MIR_SB
SDSS J172123.19+601214.5	17:21:23.10	+60:12:14.0	0.3250	2.0704	0.3099	0.10	1.04	3.26	-0.46	MIR_AGN1
SDSS J172147.65+585355.8	17:21:47.70	+58:53:55.9	0.6558	0.6585	0.6618	0.29	6.29	2.88	-0.61	MIR_SB
SSTXFLS J172151.7+585327	17:21:51.77	+58:53:27.7	0.6101	0.6159	0.6159	0.15	4.10	2.78	-1.17	MIR_SB
SSTXFLS J172218.3+584144	17:22:18.34	+58:41:44.6	0.8504	0.8587	0.8587	0.13	1.08	2.98	0.21	MIR_SB
SDSS J172301.43+594053.8	17:23:01.40	+59:40:54.0	0.5232	0.5249	0.5249	0.25	4.45	3.26	0.26	MIR_SB
SSTXFLS J172303.3+591600	17:23:03.30	+59:16:00.2	1.9510	1.9559	1.9441	0.36	7.73	2.39	-1.48	MIR_SB
NGC 6328	17:23:41.00	-65:00:37.0	0.0142	0.0141	1.7782	0.13	1.85	4.06	1.58	MIR_AGN1
3C 356	17:24:19.00	+50:57:40.0	1.0790	1.0873	1.0873	0.13	2.85	3.72	0.16	MIR_AGNx
SSTXFLS J172428.4+601533	17:24:28.44	+60:15:33.2	2.3250	2.3394	2.3394	0.08	1.29	3.02	0.23	MIR_AGN2
SDSS J172458.35+591545.8	17:24:58.30	+59:15:45.0	0.4940	0.4947	0.4947	0.28	8.51	2.97	-0.48	MIR_SB
SDSS J172704.67+593736.6	17:27:04.67	+59:37:36.6	1.1284	1.1294	1.1294	0.13	1.39	3.77	0.11	MIR_AGN1
UGC 11130	18:06:50.70	+69:49:28.0	0.0510	0.4390	0.4390	0.19	1.62	4.01	0.48	MIR_AGN1
IRAS F18216+6419	18:21:57.30	+64:20:36.0	0.2970	0.2969	0.2969	0.36	2.71	4.19	0.77	MIR_AGN1
3C 381	18:33:46.30	+47:27:03.0	0.1605	0.1595	-0.0218	0.16	2.57	4.31	1.25	MIR_AGN2
ESO 103- G 035	18:38:20.30	-65:25:39.0	0.0130	0.0141	0.0597	0.30	1.78	4.53	2.32	MIR_AGN2
CGCG 114-025	18:38:26.20	+17:11:49.7	0.0168	0.0161	0.0161	0.29	1.29	3.68	0.34	MIR_AGN2
3C 390.3	18:42:09.00	+79:46:17.0	0.0560	0.1007	0.1007	0.35	2.32	4.65	1.59	MIR_AGN1
2MASX J18470283-7831494	18:47:02.80	-78:31:50.0	0.0740	0.0746	0.0121	0.13	1.19	3.87	0.31	MIR_AGN2
ESO 141- G 055	19:21:14.10	-58:40:13.0	0.0360	0.0366	0.0618	0.10	1.75	4.42	0.76	MIR_AGN
AM 1925-724	19:31:21.40	-72:39:18.0	0.0620	0.0618	0.0576	0.41	4.01	4.51	2.17	MIR_AGN2
NGC 6810	19:43:34.40	-58:39:21.0	0.0070	0.0060	0.0060	0.48	6.63	4.22	1.45	MIR_SB
2MASX J19455354+7055488	19:45:53.50	+70:55:49.0	0.1008	0.1007	0.0985	0.24	3.84	3.46	-0.06	MIR_AGN2
Cygnus A	19:59:28.30	+40:44:02.0	0.0560	0.0555	0.0555	0.40	2.71	5.24	2.85	MIR_AGN2
IRAS 20037-1547	20:06:31.70	-15:39:08.0	0.1919	0.1924	0.1924	0.28	2.92	4.24	1.58	MIR_AGN2
NGC 6860	20:08:46.90	-61:06:01.0	0.0150	0.0121	0.0121	0.28	2.32	3.82	0.37	MIR_AGNx
NGC 6890	20:18:18.10	-44:48:25.0	0.0080	0.0080	0.0080	0.27	3.21	3.84	0.81	MIR_SB
MRK 0509	20:44:09.70	-10:43:25.0	0.0340	0.0346	0.0243	0.24	1.38	5.29	2.80	MIR_AGNx
IRAS 20414-1651	20:44:18.20	-16:40:16.0	0.0860	0.0833	0.0833	0.72	6.93	4.06	1.27	MIR_SB
3C 424	20:48:12.00	+07:01:17.5	0.1269	0.7505	1.5189	0.13	2.23	3.09	0.15	MIR_AGN1
IC 5063	20:52:02.30	-57:04:08.0	0.0110	0.0100	0.2510	0.38	2.04	4.72	2.31	MIR_AGN2
UGC 11680	21:07:43.60	+03:52:30.0	0.0260	0.0243	0.0243	0.20	1.68	3.57	0.28	MIR_AGN2

Table 1 (cont'd)

source ID (1)	RA (J2000.0) (2)	Dec (J2000.0) (3)	$z_{\rm spec}$ (4)	$z_{\rm MCPL}$ (5)	$z_{\rm ML}$ (6)	γ (7)	R (8)	$\log \mathcal{N}$ (9)	$\log \chi^2_{\rm ML}$ (10)	MIRclass (11)
UGC 11680 NED02	21:07:45.80	+03:52:40.0	0.0263	0.0304	0.0243	0.11	1.66	4.29	0.90	MIR_SB
IRAS 21208-0519	21:23:29.10	-05:06:56.0	0.1300	0.1275	0.1297	0.42	6.01	3.89	1.54	MIR_SB
2MASX J21354580-2332359	21:35:45.80	-23:32:35.0	0.1250	0.1252	0.1252	0.54	1.26	4.61	1.56	MIR_SB
IRAS 21477+0502	21:50:16.30	+05:16:03.0	0.1710	0.1711	0.1711	0.34	2.79	4.67	2.06	MIR_SB
NGC 7172	22:02:01.90	-31:52:11.0	0.0090	0.0100	0.0100	0.63	9.35	4.38	2.60	MIR_AGN2
[HB89] 2201+315	22:03:15.00	+31:45:38.0	0.2950	0.2943	0.3337	0.08	1.41	4.93	1.48	MIR_AGN1
2MASX J22041914+0333511	22:04:19.20	+03:33:50.0	0.0611	0.0576	0.1343	0.15	1.96	4.55	1.01	MIR_AGN
NGC 7213	22:09:16.20	-47:10:00.0	0.0060	0.0040	0.0040	0.16	1.23	5.22	3.44	MIR_AGN1
IRAS 22088-1832	22:11:33.80	-18:17:06.0	0.1702	0.1711	0.1711	0.74	29.54	4.27	1.50	MIR_SB
MRK 0304	22:17:12.20	+14:14:21.0	0.0660	0.0682	0.0920	0.10	1.08	4.99	1.33	MIR_AGN1
SMM J221733.02+000906.0	22:17:33.02	+00:09:06.0	0.9260	0.9268	0.9540	0.14	1.24	2.19	-0.75	unknown
NGC 7252	22:20:44.77	-24:40:41.8	0.0158	0.0161	0.0161	0.54	5.50	5.09	3.24	MIR_SB
3C 445	22:23:49.60	-02:06:12.0	0.0560	0.0387	0.0387	0.24	1.45	4.62	1.52	unknown
2MASX J22255423+1958372	22:25:54.20	+19:58:37.0	0.1470	0.1479	0.1479	0.29	2.71	4.39	0.83	MIR_AGN2
[HB89] 2225-055	22:28:30.40	-05:18:55.0	1.9810	1.8858	1.8858	0.10	1.77	4.10	0.66	MIR_AGN1
NGC 7314	22:35:46.20	-26:03:01.0	0.0050	0.0060	0.0060	0.43	3.81	4.19	1.42	MIR_AGN2
UGC 12138	22:40:17.00	+08:03:14.0	0.0250	0.0243	0.0243	0.42	6.21	4.25	1.32	MIR_SB
MCG -03-58-007	22:49:37.10	-19:16:26.0	0.0310	0.0325	0.0366	0.24	2.62	3.97	0.68	MIR_AGN1
IRAS F22491-1808	22:51:49.20	-17:52:23.0	0.0760	0.0790	0.0790	0.35	1.10	4.26	2.04	MIR_SB
[HB89] 2251+113	22:54:10.40	+11:36:38.0	0.3260	0.3743	0.3743	0.12	1.14	4.02	0.99	MIR_AGN1
NGC 7469	23:03:15.60	+08:52:26.0	0.0160	0.0161	0.0121	0.61	10.99	4.35	1.54	MIR_SB
MRK 0926	23:04:43.50	-08:41:09.0	0.0470	0.0450	0.1297	0.21	1.91	4.94	2.31	MIR_AGN2
NGC 7496	23:09:47.30	-43:25:41.0	0.0060	-0.0020	-0.0040	0.69	14.12	4.11	0.84	MIR_SB
2MASSi J2315213+260432 ID	23:15:21.40	+26:04:32.0	0.1790	0.1782	0.1782	0.74	39.43	4.11	1.06	MIR_SB
3C 459	23:16:35.20	+04:05:18.0	0.2201	0.2189	0.2165	0.22	2.43	3.62	0.70	MIR_AGN2
NGC 7582	23:18:23.50	-42:22:14.0	0.0050	0.0040	0.0040	0.71	18.35	5.71	3.46	MIR_SB
NGC 7590	23:18:55.00	-42:14:17.0	0.0050	0.0040	0.0040	0.40	2.80	3.60	1.03	MIR_SB
NGC 7603	23:18:56.60	+00:14:38.0	0.0295	0.0304	0.0304	0.31	1.82	5.21	2.88	MIR_SB
2MASX J23255611+1002500	23:25:56.20	+10:02:49.0	0.1280	0.1297	0.1297	0.49	9.57	3.99	1.21	MIR_SB
2MASX J23351192+2930000	23:35:11.90	+29:30:00.0	0.1070	0.1074	0.1118	0.32	3.49	4.19	1.70	MIR_COMP
NGC 7714	23:36:14.10	+02:09:18.6	0.0090	0.0080	0.0080	0.45	2.40	4.59	2.35	MIR_SB
NGC 7720	23:38:29.50	+27:01:55.9	0.0302	0.5007	0.2510	0.11	1.13	3.62	0.85	MIR_AGN2
2MASX J23444953+1221430	23:44:49.50	+12:21:43.0	0.1990	0.1996	0.1996	0.12	1.31	4.44	1.05	MIR_AGN1
KUG 2346+019A	23:48:41.70	+02:14:23.0	0.0310	0.0325	0.5097	0.18	1.01	3.74	0.72	MIR_SB
[HB89] 2349-014	23:51:56.10	-01:09:13.0	0.1740	0.1735	0.1758	0.18	1.72	4.27	1.26	MIR_AGN2

Note. — (1) Source identification in NED. (2),(3) J2000 right ascension and declination. (4) Spectroscopic redshift from NED. (5),(6) MCPL and ML redshift solutions, respectively. (7) Reliability parameter for MCPL solution. (8) Ratio of γ values for the first and second MCPL redshift solutions. (9) Logarithm of the net significance. (10) Logarithm of the reduced χ^2 for the ML solution. (11) MIR classification of the source.

Table 2. Infrared templates

No.	template ID	redshift	type	source
1	NGC 5011	0.00105	El-2	CWW_E + IRS[a]
2	PG 1116+215	0.1765	QSO (S1.0)	QSO_comp + IRS
3	PG 1048+342	0.16713	Elliptical (S1.0)	QSO_comp + IRS[b]
4	2MASS J12324114+1112587	0.249	NLAGN	QSO_comp + IRS
5	2MASXi J2222211+195947	0.21	Seyfert (S1.0)	IRS + IRS[c]
6	PG 1440+356	0.079	QSO (S1n)	QSO_comp + IRS
7	[HB89] 1415+451	0.1136	RQQ (S1.0)	QSO_comp + IRS
8	3C 120	0.03301	BLRG	QSO_comp + IRS
9	PG 1700+518	0.292	QSO (S1.0)	QSO_comp + IRS
10	IRAS 23060+0505	0.173	ULIRG (S1h)	AKARI + IRS
11	NGC 7674	0.02892	Seyfert (S1h)	AKARI + IRS
12	IRAS 08559+1053	0.148	ULIRG (S2)	AKARI + IRS
13	NGC 1068	0.00379	LIRG (S2)	ISO SWS
14	NGC 7130	0.01615	LIRG (S1.9)	AKARI + IRS
15	PG 0157+001	0.16311	QSO (S1.5)	QSO_comp + IRS
16	RG strong [SIV]	0.00000	RG composite	IRS composite[d]
17	ESO 339-G011	0.0192	LIRG (S2)	AKARI + IRS
18	IRAS 22206-2715	0.1314	ULIRG (HII)	AKARI + IRS
19	MCG-02-01-051	0.0271	LIRG (HII)	AKARI + IRS
20	IRAS 11582+3020	0.223	ULIRG (LINER)	AKARI + IRS
21	IRAS 12359-0725	0.138	ULIRG (HII/LINER)	AKARI + IRS
22	IRAS 12018+1941	0.1686	ULIRG (S2)	AKARI + IRS

[a] Optical-NIR elliptical galaxy template from Coleman et al. (1980).

[b] Glikman + blueAGN composite.

[c] Extended at shorter wavelengths using IRS spectrum of BAL QSO ELAISC15 J003059-442133 (z=2.101).

[d] composite spectrum of radiogalaxies with strong emission in the [SIV] 10.51 μm line.

Table 3. Reliability of redshift meassurements

γ range	N sources	$\sigma(d)$[a]	median δ[b]	$f(\delta < 0.02)$[c]	$f(\delta > 0.02)$[d]	$f(\delta > 0.1)$[e]
0.05–0.1	73	0.0279	0.0040	0.53	0.47	0.30
0.1–0.15	80	0.0204	0.0020	0.73	0.28	0.12
0.15–0.2	49	0.0131	0.0019	0.88	0.12	0.08
0.2–0.3	89	0.0084	0.0011	0.96	0.04	0.03
0.3–0.5	123	0.0056	0.0009	0.98	0.02	0.01
0.5–1.0	77	0.0020	0.0009	1.00	0.00	0.00

[a] standard deviation of redshift errors (excludes catastrophic errors).

[b] median redshift accuracy (excludes catastrophic errors).

[c] frequency of accurate redshift solutions.

[d] frequency of outliers.

[e] frequency of catastrophic errors.

Table 4. Dependency with MIR type

subset	MIR_SB	MIR_AGN	MIR_AGN1	MIR_AGN2	Total
$\delta < 0.02$	179	223	80	114	422
$\delta \geqslant 0.02$	2	62	33	10	69
$\gamma > 0.15$	175	149	54	86	338
$\gamma > 0.15$ & $\delta < 0.02$	173	139	47	85	325
$\gamma > 0.15$ & $\delta \geqslant 0.02$	2	10	7	1	13
Total	181	285	113	124	491

Table 5. Sources with accurate secondary redshift solutions

source name (1)	$z_{\rm spec}$ (2)	$z_{\rm MCPL}$ (3)	$z_{\rm alt}$ (4)	$d_{\rm alt}$ (5)	$\gamma_{\rm alt}$ (6)	# (7)	P$_r$ (8)
[HB89] 1435-067	0.1260	0.0768	0.1343	0.0073	0.017	20	0.2059
[HB89] 1543+489	0.3996	0.8662	0.4077	0.0058	0.052	6	0.0584
2MASSi J1516532+190048	0.1900	0.2386	0.1924	0.0020	0.053	6	0.0265
2MASSi J1649149+530316	2.2600	2.5317	2.2084	-0.0158	0.081	2	0.0390
2MASX J00215355-7910077	0.0728	0.0304	0.0725	-0.0003	0.090	2	0.0020
2MASX J01500266-0725482	0.0180	0.0876	0.0182	0.0002	0.186	3	0.0012
2MASX J14025121+2631175	0.1870	0.1185	0.1641	-0.0193	0.071	5	0.1313
3C 015	0.0730	3.3134	0.0725	-0.0005	0.045	13	0.0076
3C 076.1	0.0324	0.8812	0.0366	0.0041	0.060	2	0.0102
3C 424	0.1269	0.7505	0.1230	-0.0035	0.044	5	0.0215
4C +29.31	0.3980	1.8457	0.3993	0.0009	0.070	2	0.0022
APMUKS(BJ) B003833.18-442916.3	1.3800	0.6618	1.4105	0.0128	0.064	2	0.0316
B3 1635+416	1.1790	1.0055	1.1423	-0.0169	0.085	3	0.0616
ELAISC15 J003014-430332	1.6540	1.3770	1.6480	-0.0022	0.067	2	0.0056
FLX J142644.33+333051.7	3.3550	1.5391	3.3568	0.0004	0.074	3	0.0015
GALEX 2533910445613399575	1.7070	1.9677	1.7069	-0.0000	0.087	4	0.0001
GOODS J123600.15+621047.5	2.0020	0.4593	2.0156	0.0045	0.037	7	0.0388
LBQS 0018-0220	2.5960	0.8183	2.5958	-0.0001	0.062	3	0.0002
MESSIER 058	0.0050	0.5218	0.0040	-0.0010	0.136	2	0.0055
MM J163655+4059	2.5920	3.1031	2.6030	0.0031	0.084	2	0.0076
MRK 0704	0.0290	0.5619	0.0304	0.0014	0.175	3	0.0111
MRK 1298	0.0620	0.3688	0.0768	0.0140	0.044	9	0.2177
NGC 2484	0.0408	0.4332	0.0387	-0.0020	0.034	17	0.0414
PG 0052+251	0.1550	0.1252	0.1479	-0.0061	0.098	3	0.0308
PG 1004+130	0.2410	0.1434	0.2287	-0.0099	0.036	9	0.1430
PICTOR A	0.0340	0.0040	0.0408	0.0066	0.139	2	0.0255
SBS 1408+567	2.5830	2.7500	2.5246	-0.0163	0.030	11	0.2045
SDSS J012341.46+004435.9	0.3990	2.2602	0.4105	0.0082	0.069	2	0.0203
SDSS J103951.48+643004.2	0.4020	1.0831	0.4049	0.0020	0.082	2	0.0053
SDSS J123716.59+621643.9	0.5570	1.8061	0.5495	-0.0048	0.088	2	0.0120
SDSS J160250.95+545057.8	1.1970	0.3073	1.1943	-0.0012	0.053	3	0.0046
SDSS J161007.11+535814.0	2.0150	1.8800	2.0216	0.0022	0.037	12	0.0323
SDSS J161526.63+543005.9	1.3670	1.1681	1.4009	0.0143	0.054	3	0.0525
SDSS J163721.21+411502.7	2.3560	3.1031	2.3061	-0.0149	0.065	7	0.1224
SDSS J163739.43+414348.0	1.4140	0.9346	1.4153	0.0006	0.041	11	0.0075
SDSS J163847.42+421141.7	1.7710	1.6961	1.8118	0.0147	0.040	8	0.1373
SDSS J163952.85+410344.8	1.6030	1.5240	1.5595	-0.0167	0.068	4	0.0805
SDSS J164016.08+412101.2	1.7620	1.1638	1.8061	0.0160	0.041	8	0.1484
SDSS J171313.96+603146.5	0.1050	0.1900	0.1163	0.0102	0.081	2	0.0252
SDSS J171324.17+585549.1	0.6090	0.6420	0.6095	0.0003	0.056	4	0.0015
SDSS J171748.42+594820.6	0.7630	0.7262	0.7646	0.0009	0.053	3	0.0033
SDSS J171902.28+593715.9	0.1783	0.1118	0.1829	0.0039	0.015	20	0.0964
SDSS J172123.19+601214.5	0.3250	2.0704	0.3099	-0.0114	0.098	2	0.0282
SST24 J143424.4+334543	2.2630	2.3729	2.2537	-0.0029	0.085	2	0.0071
SWIRE J104406.30+583954.1	2.4300	3.8730	2.3797	-0.0147	0.029	9	0.1528
SWIRE J104409.95+585224.8	2.5400	0.4247	2.5387	-0.0004	0.045	3	0.0013
SWIRE4 J002959.22-434835.1	2.0390	2.1324	2.0156	-0.0077	0.050	5	0.0470
UGC 00595	0.0450	0.3826	0.0471	0.0020	0.060	7	0.0171

Note. — (1) Source identifier in NED. (2) Optical spectroscopic redshift. (3) MCPL redshift solution. (4) Redshift of secondary MCPL solution that matches $z_{\rm spec}$. (5) Redshift error for secondary solution. (6) Reliability parameter for secondary solution. (7) Order number of the secondary solution after sorting by decreasing γ values. (8) Probability of secondary solution being spurious.